

The Acoustic Resonant Drag Instability with a Spectrum of Grain Sizes

Jonathan Squire¹, Stefania Moroianu², & Philip F. Hopkins³

¹Physics Department, University of Otago, Dunedin 9010, New Zealand

²Department of Applied Physics, Stanford University, Stanford, CA 94305, USA

³TAPIR, Mailcode 350-17, California Institute of Technology, Pasadena, CA 91125, USA

Submitted to MNRAS, 2021

ABSTRACT

We study the linear growth and nonlinear saturation of the “acoustic Resonant Drag Instability” (RDI) when the dust grains, which drive the instability, have a wide, continuous spectrum of different sizes. This physics is generally applicable to dusty winds driven by radiation pressure, such as occurs around red-giant stars, star-forming regions, or active galactic nuclei. Depending on the physical size of the grains compared to the wavelength of the radiation field that drives the wind, two qualitatively different regimes emerge. In the case of grains that are larger than the radiation’s wavelength – termed the *constant-drift* regime – the grain’s equilibrium drift velocity through the gas is approximately independent of grain size, leading to strong correlations between differently sized grains that persist well into the saturated nonlinear turbulence. For grains that are smaller than the radiation’s wavelength – termed the *non-constant-drift* regime – the linear instability grows more slowly than the single-grain-size RDI and only the larger grains exhibit RDI-like behavior in the saturated state. A detailed study of grain clumping and grain-grain collisions shows that outflows in the constant-drift regime may be effective sites for grain growth through collisions, with large collision rates but low collision velocities.

Key words: instabilities – turbulence – ISM: kinematics and dynamics – galaxies: formation – stars: winds, outflows – dust, extinction

1 INTRODUCTION

Cosmic dust is ubiquitous across the universe and vital to a wide range of astrophysical processes. By mass, it makes up around $\sim 1\%$ of the interstellar medium (ISM) of galaxies, but its strong coupling to radiation fields implies it can nonetheless strongly influence gas dynamics and cooling in many situations (Draine 2010). More generally, because around half of the metal content of our galaxy is locked up in dust, it plays crucial roles in any process that requires metals or solids (Whittet 1992; Draine 2003). Notably, dust is almost certainly the key ingredient for planet formation and life, supplying the necessary reservoir of solids that provide the seeds to make planetesimals in protostellar disks (Chiang & Youdin 2010).

This paper deals with the physics of dust moving through gas, with the interaction between the species mediated by drag forces. Such conditions occur, for example, in dust-radiation-pressure driven winds, where an outflow of dusty gas is driven by an anisotropic radiation field that couples strongly to the dust. Such outflows are thought to be important in the evolution of asymptotic giant-branch (AGB) stars (which also produce large quantities of dust; e.g., Habing 1996; Norris et al. 2012), in feedback processes that help regulate star formation and/or active-galactic nuclei (Scoville 2003; Thompson et al. 2005; Ishibashi & Fabian 2015), around supernovae (e.g., Micelotta et al. 2018), and in the bulk ISM (Weingartner & Draine 2001b) and circum-galactic medium (CGM; Ménard et al. 2010). As shown by Squire & Hopkins (2018a), this situation – specifically, when the radiation pressure on the dust is stronger than that on the gas, such that the gas

outflow is driven indirectly through the drag force from the dust – is unstable to the “Resonant Drag Instability” (RDI): small perturbations in the gas or dust will grow in time until they become large, driving turbulence in the gas and strong dust clumping. Hopkins & Squire (2018a) (hereafter HS18) studied the linear features and growth rates of the RDI for the case of nearly neutral grains and neutral gas in outflows, while Hopkins & Squire (2018b) generalized these results to charged grains in magnetized gas. These results were then extended to the nonlinear regime by Moseley et al. (2019) (hereafter MSH19) and Seligman et al. 2019; Hopkins et al. 2020 (in the magnetized regime), who studied the turbulence induced by the RDI, constructing simple estimates for its saturation amplitude and other properties.

However, each of these studies has allowed for the dust grains to have only a single size. As shown by Krapp et al. (2019); Paardekooper et al. (2020); Zhu & Yang (2021) for the streaming instability in protoplanetary disks (which is part of the RDI family; Squire & Hopkins 2018b), a range of grain sizes can strongly influence the instabilities in some regimes. Thus, for more realistic application to astrophysical fluids and outflows, where the range in grain sizes easily spans two orders of magnitude or more (Draine 2010), we must relax the single-grain-size assumption and better understand the influence of a spectrum of grain sizes on the growth rate and saturation of the RDI. This is the first purpose of the present paper. We study both the linear growth rates and nonlinear saturation of the “acoustic RDI” (HS18) that applies to uncharged grains and neutral gas, and involves the driving of compressive shocks and sound waves by the drifting dust. We find that depending on whether grains are smaller or larger than the wave-

length of the accelerating radiation field, the presence of a spectrum of grains either has little effect on the acoustic RDI or reduces the growth rate and saturation of smaller-scale motions. In both cases, key features of the linear-instability structure persist well into the highly turbulent saturated state.

The second purpose of this paper is to better understand dust clumping and collisions in RDI turbulence (i.e., the saturated state of the acoustic RDI). This is important because outflows are highly dynamic and often thought to be key sites for grain condensation, coagulation, and fragmentation, and the latter two of these processes are strongly influenced by turbulence. While well developed theories exist to describe the how standard gas turbulent motions influence dust collisions (e.g., Ormel & Cuzzi 2007; Pan & Padoan 2013; Pumir & Wilkinson 2016), the structure of the turbulence and clumping driven by the acoustic RDI is quite different to standard turbulence in many ways, because the instability operates across all scales of the system simultaneously (MSH19). In this context, it is important to consider the RDI with a wide spectrum of grain sizes (as opposed to the single-grain-size RDI) because the nature of the instability suggests that there could exist interesting correlations between differently sized grains in some regimes, and grain clumping and collision statistics depend strongly on grain sizes (Pan et al. 2014b; Blum 2018; Mattsson et al. 2019). With this in mind, our nonlinear study is designed to compare RDI saturation to forced turbulence with passively advected dust. We do this by designing “equivalent” forced turbulence simulations (i.e., simulations with parameters chosen to match the saturated RDI as closely as possible), allowing an explicit comparison of the statistics of dust in RDI turbulence with those of passive dust in forced turbulence. Given the rather detailed nature of these comparisons, we focus on just two RDI case studies at the high numerical resolution, but with parameters that can be applicable to a range of astrophysical scenarios. Depending on the regime, we find that the RDI involves a significantly faster rate of lower-velocity collisions than forced turbulence, particularly between grains of different sizes. It also exhibits far stronger clumping of the smallest grains, even when simple estimates suggest these small grains should be very well coupled to the gas.

The paper is split in two: first the main exposition; second an extended appendix that studies analytically the linear behavior of the acoustic RDI with a spectrum of grain sizes. This split was chosen because the linear calculations, in which we derive simple analytic expressions for the RDI growth rate in most of the important regimes, are necessarily rather technical. They do provide useful understanding of the nonlinear behavior, however, so we will refer to those results throughout. The main paper starts in § 2 with a detailed description of the problem, model, and numerical setup, particularly focusing on important differences that arise in the dust (quasi-)equilibrium depending on the wavelength of the radiation compared to the dust size (§ 2.2 and Tab. 1). The numerical results are presented in § 3, starting with a discussion of the broad morphological features of the turbulence and how this differs between regimes and driving (§ 3.1), then followed by a more detailed analysis of the grain clumping and collisions (§§ 3.2 and 3.3).

2 NUMERICAL MODEL AND PHYSICAL SETUP

2.1 Dust and gas model

We model gas dynamics using the standard neutral fluid equations, ignoring magnetohydrodynamic effects and charged grains for simplicity in this study, although such effects are important for many

astrophysical regimes (HS18). Dust is modelled numerically by treating it as a population of individual particles (the super-particle approach), which interact with the gas through drag forces that depend on the grain size. We use $f_d(\epsilon_{\text{grain}}; \mathbf{x}, \mathbf{v}, t)$ to denote the phase-space density of grains with radius ϵ_{grain} , velocity \mathbf{v} , at position \mathbf{x} , such that the equations of motion are

$$\begin{aligned} \frac{\partial \rho_g}{\partial t} + \nabla \cdot (\rho_g \mathbf{u}_g) &= 0, \quad (1) \\ \frac{\partial \mathbf{u}_g}{\partial t} + \mathbf{u}_g \cdot \nabla \mathbf{u}_g &= -c_s^2 \frac{\nabla \rho_g}{\rho_g} + \frac{1}{\rho_g} \int d\epsilon_{\text{grain}} d\mathbf{v} f_d(\mathbf{x}, \mathbf{v}, \epsilon_{\text{grain}}) \frac{\mathbf{v} - \mathbf{u}_g}{t_s(\epsilon_{\text{grain}}, \mathbf{v})}, \quad (2) \\ \frac{\partial f_d}{\partial t} + \mathbf{v} \cdot \nabla f_d + \frac{\partial}{\partial \mathbf{v}} \cdot \left[\left(-\frac{\mathbf{v} - \mathbf{u}_g(\mathbf{x})}{t_s(\epsilon_{\text{grain}}, \mathbf{v})} + \mathbf{a}^{\text{ext}}(\epsilon_{\text{grain}}) \right) f_d \right] &= 0. \quad (3) \end{aligned}$$

Given the super-particle approach, the final equation is equivalent to modeling individual grains of size $\epsilon_{\text{grain},j}$, with velocity \mathbf{v}_j and position \mathbf{x}_j , with

$$\frac{\partial \mathbf{x}_j}{\partial t} = \mathbf{v}_j, \quad \frac{\partial \mathbf{v}_j}{\partial t} = -\frac{\mathbf{v}_j - \mathbf{u}_g(\mathbf{x}_j)}{t_s(\epsilon_{\text{grain},j}, \mathbf{v}_j)} + \mathbf{a}^{\text{ext}}(\epsilon_{\text{grain},j}) \quad (4)$$

as they move through the gas velocity field, then constructing f_d by counting dust particles at each gas position. Here ρ_g is the gas density, \mathbf{u}_g is the gas velocity, c_s is the sound speed (the equation of state is taken as isothermal), $t_s(\epsilon_{\text{grain}}, \mathbf{v})$ is the stopping time (see Eq. (7) below), and \mathbf{a}^{ext} is an external force from radiation pressure on the grains, which we will take (arbitrarily) to be in the $\hat{\mathbf{z}}$ direction $\mathbf{a}^{\text{ext}} = a^{\text{ext}} \hat{\mathbf{z}}$ (see § 2.2). The final term in Eq. (2) is the dust “backreaction” force – it the force on the gas from the dust – which is neglected in most studies of dust dynamics. We also use $\langle \cdot \rangle$ to denote the volume average, and the subscripts \perp and \parallel to denote velocities in the directions perpendicular and parallel to the mean drift, respectively (e.g., $\langle u_{g,\parallel}^2 \rangle = \langle u_{g,z}^2 \rangle$, $\langle u_{g,\perp}^2 \rangle = \langle u_{g,x}^2 + u_{g,y}^2 \rangle$). A δ indicates that the mean is subtracted from a quantity before averaging (e.g., $\delta v_{d,\parallel} = v_{d,\parallel} - \langle v_{d,\parallel} \rangle$). All quantities will be measured in the frame where the gas is stationary ($\mathbf{u}_g = 0$).

To understand dust dynamics, analyze simulations, and compute linear growth rates, it is helpful to take the zeroth and first velocity moments of f_d , defining

$$\rho_d = \int_{\epsilon_{\text{gr},l}}^{\epsilon_{\text{gr},h}} d\epsilon_{\text{grain}} d\mathbf{v} f_d, \quad \mathbf{v}_d = \frac{1}{\rho_d} \int_{\epsilon_{\text{gr},l}}^{\epsilon_{\text{gr},h}} d\epsilon_{\text{grain}} d\mathbf{v} \mathbf{v} f_d, \quad (5)$$

where the integration limits $\epsilon_{\text{gr},l}$ and $\epsilon_{\text{gr},h}$ can be taken over just a subset of grains (if specified as such; see § 2.4.2), or the full distribution (if unspecified). We use μ_0 to denote the total average dust-to-gas-mass ratio $\mu_0 = \langle \rho_d \rangle / \langle \rho_g \rangle$, and

$$w_s(\epsilon_{\text{grain}}) = \frac{\langle |v_d(\epsilon_{\text{grain}}) - \mathbf{u}_g| \rangle}{c_s}, \quad (6)$$

to denote the mean drift between dust of size ϵ_{grain} and the gas (here $v_d(\epsilon_{\text{grain}})$ is computed from $\epsilon_{\text{gr},l} = \epsilon_{\text{grain}}$, $\epsilon_{\text{gr},h} = \epsilon_{\text{grain}} + d\epsilon_{\text{grain}}$ in Eq. (5)).

Throughout, we assume Epstein drag, using the simple approximation of (Draine & Salpeter 1979),

$$t_s(\epsilon_{\text{grain}}, \mathbf{v}) = \sqrt{\frac{\pi}{8}} \frac{\bar{\rho}_{d,\text{int}} \epsilon_{\text{grain}}}{\rho_g c_s} \left(1 + \frac{9\pi}{128} \frac{|\mathbf{v} - \mathbf{u}_g|^2}{c_s^2} \right)^{-1/2}, \quad (7)$$

where $\bar{\rho}_{d,\text{int}}$ is the internal grain density. Epstein drag is generally appropriate for astrophysical conditions in which MHD and charging effects can be neglected as done here (generally, for cooler, denser gas; see, e.g., HS18).

2.1.1 Grain mass distribution

We will assume a simple power law distribution of grain sizes between $\epsilon_{\text{grain}} = \epsilon_{\text{grain}}^{\text{min}}$ and $\epsilon_{\text{grain}} = \epsilon_{\text{grain}}^{\text{max}}$. In order to reduce the number of free parameters, we use the standard MRN distribution (Mathis et al. 1977), which postulates that the mass of grains $d\mu$ within logarithmic range of sizes $d \ln \epsilon_{\text{grain}}$ is $d\mu/d \ln \epsilon_{\text{grain}} \propto \epsilon_{\text{grain}}^{0.5}$, such that most of the mass is in the largest grains, along with the total dust-to-gas-mass ratio $\mu_0 \approx 0.01$. The original distribution postulates that $\epsilon_{\text{grain}}^{\text{min}} \approx 5\text{nm}$ and $\epsilon_{\text{grain}}^{\text{max}} \approx 0.25\mu\text{m}$, although subsequent works have suggested that this underestimates significantly the population of small grains and misses a population of larger grains, even in the diffuse ISM (Weingartner & Draine 2001a; Zubko et al. 2004; Draine & Fraisse 2009). Less is known about the grain distribution in more dynamic environments (e.g., around AGB stars or the AGN dusty torus, see, e.g., Höfner & Olofsson 2018; Murray et al. 2005), where our simulations can apply by virtue of their dimensionless nature (see § 2.5 below). Cursory lower-resolution tests of different grain-mass distributions (e.g., small-grain dominated, $d\mu/d \ln \epsilon_{\text{grain}} \propto \epsilon_{\text{grain}}^{-0.5}$) have not revealed significant differences, so we shall not explore this in detail. It is, however, worth noting that for the gas of the protoplanetary-disk streaming instability, the grain distribution can affect important details of the linear instability (Paardekooper et al. 2020; McNally et al. 2021; Zhu & Yang 2021), so this issue may be worth revisiting in more detail in future work.

2.2 Grain acceleration regimes

The acoustic RDI requires a net drift between grains and the gas as their energy source. As discussed extensively in HS18 and Hopkins & Squire (2018b), such a net drift is expected to occur generically in the presence of radiation fields, which couple to the grains more strongly than to the gas under most conditions (e.g., Weingartner & Draine 2001b; Murray et al. 2005), sourcing the \mathbf{a}^{ext} term in Eq. (3). In this radiatively driven situation, two acceleration regimes naturally emerge, applying respectively to grains smaller or larger than the wavelength of the accelerating radiation λ_{rad} . The different scaling of $w_s(\epsilon_{\text{grain}})$ has important implications for the development of instabilities. Some basic properties of the different regimes are summarized in Tab. 1 for quick reference.

A coherent radiation field of energy density e_{rad} causes a grain acceleration $\mathbf{a}^{\text{ext}} \sim Q_{\text{abs}} e_{\text{rad}} \epsilon_{\text{grain}}^2 / m_d c^2$, where $m_d = 4/3 \pi \bar{\rho}_d \epsilon_{\text{grain}}^3$ is the grain’s mass. The factor Q_{abs} is the absorption efficiency; $Q_{\text{abs}} \sim 1$ if $\epsilon_{\text{grain}} \gg \lambda_{\text{rad}}$, while $Q_{\text{abs}} \sim \epsilon_{\text{grain}} / \lambda_{\text{rad}}$ if $\epsilon_{\text{grain}} \ll \lambda_{\text{rad}}$ (Weingartner & Draine 2001b). Thus, large grains in shorter wavelength radiation fields feel an acceleration $\mathbf{a}^{\text{ext}} \propto \epsilon_{\text{grain}}^{-1}$, while small grains in longer wavelength radiation fields feel an acceleration that is independent of ϵ_{grain} . In such a driven situation, the (quasi-)equilibrium occurs when the acceleration and drag forces on grains balance,¹ viz., when

$$\frac{w_s(\epsilon_{\text{grain}}, v_d)}{t_s(\epsilon_{\text{grain}}, v_d)} = \mathbf{a}^{\text{ext}}(\epsilon_{\text{grain}}). \quad (8)$$

Because $t_s(\epsilon_{\text{grain}}, v_d) \propto \epsilon_{\text{grain}}$, this implies that w_s is independent of

¹ Note that this is not actually a true equilibrium because it occurs with the system as a whole (gas and dust) accelerating linearly at a constant rate, unless \mathbf{a}^{ext} can be balanced by another external force on both gas and dust (e.g., gravity). However, this subtlety does not make a difference to the arguments here or to our simulations. The issue is discussed in detail in HS18.

grain size if $\epsilon_{\text{grain}} \gg \lambda_{\text{rad}}$, which we term the *constant drift* regime; the opposite regime, where $w_s(\epsilon_{\text{grain}})$ is a function of grain size (for $\epsilon_{\text{grain}} \ll \lambda_{\text{rad}}$) is termed the *non-constant drift* regime. In the latter case, we see from Eqs. (7) and (8) that for subsonic drift $w_s \ll 1$, t_s in the saturated state is independent of w_s so that $t_s \propto \epsilon_{\text{grain}}$ and $w_s \propto \epsilon_{\text{grain}}$, while for supersonic drift $w_s \gg 1$ (the case of more relevance to this article), the decrease in t_s with w_s implies that $t_s \propto \epsilon_{\text{grain}}^{1/2}$ and $w_s \propto \epsilon_{\text{grain}}^{1/2}$. Of course, in many physical situations, the distribution of grain sizes could fall around λ_{rad} (i.e., $\epsilon_{\text{grain}}^{\text{min}} < \lambda_{\text{rad}} < \epsilon_{\text{grain}}^{\text{max}}$), in which case the larger grains will lie in the constant-drift regime and the smaller grains in the non-constant-drift regime. However, given that our goal here is to explore the basic physics of the multi-grain RDI, we will not consider such situations in detail in this work.

A net drift of grains can also be set up through a force on the gas (and not the dust), due to radiation pressure absorbed by gas (e.g., line pressure) or gravity (e.g., in a stratified medium). In this case, the situation is identical to the non-constant-drift regime. This physics is applicable, albeit with a different linear instability, to the polydisperse streaming instability in protoplanetary disks (Krapp et al. 2019).

Note that Hopkins et al. (2021) also explore the RDI with a spectrum of grain sizes, explicitly including vertical stratification and more complex radiation-MHD effects. For some cases, they also consider simulation variants in the $\epsilon_{\text{grain}} \gg \lambda_{\text{rad}}$ and $\epsilon_{\text{grain}} \ll \lambda_{\text{rad}}$ regimes. Rather than using the labels “constant-drift” and “non-constant-drift,” they label the $\epsilon_{\text{grain}} \ll \lambda_{\text{rad}}$ (non-constant-drift) regime simulations with “-Q,” to signify that Q_{abs} depends on ϵ_{grain} in this regime. This different nomenclature is used because most of their simulations use explicit radiation-MHD effects, which leads to more complex relations between w_s and ϵ_{grain} that depend on the dynamics of the radiation field.

2.3 Behavior of the acoustic Resonant Drag Instability

As discussed in detail in Squire & Hopkins (2018a), HS18, and MSH19, the acoustic RDI exhibits different behaviors based on a dimensionless scale parameter $k c_s t_s$, where k is the wavenumber of the mode. In App. A, we cover in detail the linear behavior of the acoustic RDI with a spectrum of grain sizes, showing, as expected, that the same parameter (which now covers a range of values because of the range in ϵ_{grain}) has a similar influence on the instability. Specifically, three regimes emerge: the instability is in the low- k regime if $k c_s t_s \lesssim \mu$; the mid- k regime if $\mu \lesssim k c_s t_s \lesssim \mu^{-1}$; and the high- k regime if $\mu^{-1} \lesssim k c_s t_s$. With a spectrum of grains, there is ambiguity surrounding these delineations (t_s and μ depend on ϵ_{grain}), but they are nonetheless useful for general understanding (see App. A for more precise estimates). In the low- k regime, the fastest growing modes are generally non-resonant and grow in the direction aligned with the drift, involving strong perturbations to both the gas and dust densities. We show in App. A3.1 that such modes are generally agnostic to the presence of a spectrum of grain sizes or the drift regime (constant versus non-constant). In contrast, modes in the mid- and high- k regimes are fastest growing at a specific “resonant” mode direction, where the projection of the dust drift speed onto that direction is equal to the sound speed. They have a much stronger dust-density response than gas-density response. Such modes behave similarly in the constant-drift regime with a spectrum of grain sizes, but are significantly modified in the non-constant-drift regime because each grain size resonates with a different mode angle (see App. A3).

In addition to the linear behavior, the three regimes control

<i>Constant drift regime</i>	<i>Non-constant drift regime</i>
$\lambda_{\text{rad}} < \epsilon_{\text{grain}}, Q_{\text{abs}} \sim 1$ (radiative force on the dust)	$\lambda_{\text{rad}} > \epsilon_{\text{grain}}, Q_{\text{abs}} \sim \epsilon_{\text{grain}}/\lambda_{\text{rad}}$ (force on the dust) <i>or</i> acceleration of the gas
$a^{\text{ext}} \propto \epsilon_{\text{grain}}^{-1}$	$a^{\text{ext}} \sim \text{const.}$
$w_s \sim \text{const.}, t_s \propto \epsilon_{\text{grain}}$	$w_s \propto \epsilon_{\text{grain}}^{1/2}, t_s \propto \epsilon_{\text{grain}}^{1/2}$ (supersonic drift); $w_s \propto \epsilon_{\text{grain}}, t_s \propto \epsilon_{\text{grain}}$ (subsonic drift)
Linear instability similar to single-grain-size case	Range of resonant angles changes character of linear instability
Strong correlations between grains of different sizes in saturated state	Grain correlations broadly similar to externally forced turbulence

Table 1. Summary of some basic properties of the grains and the RDI in the constant- and non-constant-drift regimes.

the acoustic RDI’s nonlinear evolution (MSH19). While gas motions and dust clumping driven by the acoustic RDI in the low- k regime broadly resemble standard driven supersonic turbulence (although there are distinct differences), the mid- and high- k regimes are very different, with the resonant mode structure remaining clear well into the saturated state and across all scales. In larger- w_s cases, this manifests itself through thin dust filaments, which “draft” on the nearby dust and never reach a saturated turbulent steady state. For subsonic drift, the linear and nonlinear behavior is most similar to the low- k regime (indeed, the subsonic instability at mid- to high- k is non-resonant and depends on details of the equation of state and drag law; HS18).

Finally, it is worth reiterating from previous works that the acoustic RDI generally has no preferred scale in any of the three regimes. Rather, modes at smaller scales grow faster, with the growth rate $\Im(\omega)$ scaling as $\Im(\omega) \sim k^{2/3}$, $\Im(\omega) \sim k^{1/2}$, and $\Im(\omega) \sim k^{1/3}$, in the low-, mid-, and high- k regimes, respectively. Thus, simulations cannot be converged in the conventional sense, in that a higher-resolution simulation will resolve faster-growing modes (in the absence of a small-scale dissipative effect such as viscosity). However, as shown by MSH19 (appendix B3), the bulk properties of the saturated state are effectively resolution independent once box-scale modes saturate nonlinearly.

2.4 Simulation design

We use the code GIZMO,² which solves the fluid equations using the second-order Lagrangian “Meshless Finite Volume” (MFV) method (Hopkins 2015). Dust is included via the super-particle approach (Youdin & Johansen 2007; Hopkins & Lee 2016), using a random sampling of grain sizes ϵ_{grain} across the full continuous distribution (i.e., we do not use a set number of grain-size bins). The backreaction force of the dust on the gas is computed using a standard momentum-conserving scheme (Youdin & Johansen 2007), with details of the scheme and a variety of numerical tests described in appendix B of MSH19 (although MSH19 considers only a single grain size, there are no significant numerical complications that arise from the use of a spectrum of grains).

The range of available parameter space for simulations using a grain-size spectrum is extensive, even without magnetization and grain charge: it includes the drift-velocity regimes (constant versus non-constant, supersonic versus subsonic, and mixtures of each), stopping-time distributions (which could straddle the different k regimes), the distribution of grain masses, and the total dust-to-gas-mass ratio. Because of this, and motivated by the goal of better understanding RDI-turbulence physics rather than detailed matching of specific astrophysical situations, we choose in this article to

focus on the detailed understanding of just two sets of RDI parameters. We supplement this by comparing these directly to simulations without dust backreaction ($\mu_0 = 0$), where turbulence is driven by large-scale external forcing to have a similar velocity dispersion. The purpose of this comparison is two fold: firstly, and most importantly, it enables us to probe the physics of dust clumping in RDI-generated turbulence by direct comparison to the better-understood case of standard (Kolmogorov) turbulence, revealing clearly their most important differences. Secondly, in application to AGB-star winds or AGN outflows, the forced-turbulence simulation could provide a reasonable model for dust clumping if the RDI were not operating. Specifically, one might expect larger-scale global instabilities (e.g., Rayleigh-Taylor-like instabilities; Krumholz & Thompson 2012) to drive turbulence, which would then, through a turbulent cascade, drive fluctuations on the small scales considered here. Thus, the simulations act as a benchmark for how such a dust-driven wind might clump dust in the absence of RDIs (e.g., at extremely small dust-to-gas ratios), although we caution that the magnitude of the turbulent driving is not at all tuned to explore this in detail (rather it is tuned to address the first point and probe the physics).

The overall approach complements and builds on that of MSH19 and Hopkins et al. (2020), which surveyed a wide range of parameters to understand how the RDI behaves in different regimes. Specifically, the results of MSH19 tell us that the most interesting computationally accessible RDI behaviour – i.e., that which exhibits the most interesting differences compared to standard turbulence – occurs in the “mid- k ” range. As discussed above (§2.3) this regime is also expected to show more interesting differences between the grain-spectrum and single-grain RDIs, so is, overall, the most obvious candidate for further study.³ Thus we will ignore the low- k regime and/or subsonic drift in this study. Although they are potentially astrophysically relevant in many situations (Hopkins et al. 2021), these regimes can likely be mostly adequately understood using a combination of RDI-related understanding from MSH19 and HS18 and theories of collisions/clustering in turbulence with a spectrum of sizes without dust backreaction (e.g., Pan et al. 2014b; Pan & Padoan 2014; Hopkins & Lee 2016; Mattsson et al. 2019; Li & Mattsson 2020).

Based on the discussion of the previous paragraph, we focus on four simulations with a grain-size spectrum covering a factor of 100 ($\epsilon_{\text{grain}}^{\text{max}} = 100\epsilon_{\text{grain}}^{\text{min}}$), each in a cubic box of size L^3 . These are:

Constant-Drift RDI This simulation sets $a^{\text{ext}} \propto 1/\epsilon_{\text{grain}}$ such that w_s is independent of ϵ_{grain} and $t_s \propto \epsilon_{\text{grain}}$. The acceleration and

³ Unfortunately, reaching the true high- k regime has proved to be computationally challenging, because the width of the resonant wavelengths become increasingly narrow at increasing k , necessitating excessively high resolution. MSH19 considered some cases around the boundary between the mid- and high- k regimes, which were similar to the mid- k cases (see their appendix A for more information).

² A public version of the code, including all methods used in this paper, is available at <http://www.tapir.caltech.edu/phopkins/Site/GIZMO.html>

grain size range (see below) is chosen such that $w_s \approx 1.5$, which is convenient because the resonant angle at which the modes grow fastest ($\cos \theta_k = 1/w_s$) is neither too oblique nor too parallel, as well as being astrophysically reasonable. The outer-scale normalized wavenumbers of grains range from $(2\pi/L)c_s t_s \approx 0.005$ to $(2\pi/L)c_s t_s \approx 0.5$.

No-Backreaction Constant Drift This simulation has parameters (including a^{ext}) that match exactly Constant Drift RDI, but with no dust backreaction, and thus no RDI. Instead, the turbulence is externally driven, with the amplitude of the forcing chosen so that the resulting turbulence has a velocity dispersion that matches (as closely as possible) the Constant Drift RDI simulation.

Non-Constant-Drift RDI This simulation sets a^{ext} constant such that w_s and t_s both depend on ϵ_{grain} ($Q_{\text{abs}} \sim \epsilon_{\text{grain}}/\lambda_{\text{rad}}$). The acceleration and grain size range is chosen such that $w_s \sim \epsilon_{\text{grain}}^{1/2}$ ranges between $w_s \approx 0.73$ (for the smallest grains) and $w_s \approx 12.7$ (for the largest grains). The outer-scale normalized wavenumbers of grains range from $(2\pi/L)c_s t_s \approx 0.003$ to $(2\pi/L)c_s t_s \approx 0.05$ (note that $t_s \sim \epsilon_{\text{grain}}^{1/2}$ for the larger/faster grains).

No-Backreaction Non-Constant Drift This simulation has parameters (including a^{ext}) that match exactly Non-Constant Drift RDI, but with no dust backreaction and using external driving to match the turbulence amplitude of Non-Constant Drift RDI.

Note that in each case, $(2\pi/L)c_s t_s < 1$ is chosen so that smaller-scale modes in the box do not move too far into the high- k regime, where they may be adversely affected by numerical resolution. In the non-constant drift cases, the range in w_s is chosen so that most grains are supersonic, but the largest grains are not highly supersonic (w_s not too much larger than ≈ 10), which was shown by MSH19 to cause particularly extreme behavior (drafting) that does not necessarily converge in time (owing in part due to the finite periodic box assumption that we adopt). The equilibrium w_s and $(2\pi/L)c_s t_s$ are shown below in the insets of Figs. 2 and 4.

2.4.1 Numerical parameters

In each case, it is convenient to use code units defined by $\langle \rho_g \rangle = 1$, $c_s = 1$, $\bar{\rho}_{d,\text{int}} = 1$, and $L = 1$. Then, $w_s(\epsilon_{\text{grain}})$ and $t_s(\epsilon_{\text{grain}})$ are numerically determined by the combination of ϵ_{grain} and a^{ext} (in code units); in order to obtain the simulation parameters discussed above, we need $\epsilon_{\text{grain}}^{\text{max}} = 0.15 = 100\epsilon_{\text{grain}}^{\text{min}}$ with $a^{\text{ext}} = 3/\epsilon_{\text{grain}}$ for the constant-drift simulations, and $\epsilon_{\text{grain}}^{\text{max}} = 0.0878 = 100\epsilon_{\text{grain}}^{\text{min}}$ with $a^{\text{ext}} = 1400$ for the non-constant-drift simulations. Grains are initialized with their equilibrium drift velocity ($w_s(\epsilon_{\text{grain}})/t_s(\epsilon_{\text{grain}}) = a^{\text{ext}}$), which is also present in the driven cases without backreaction (unlike previous studies of turbulent grain dynamics). We use periodic boundary conditions with a resolution of 256^3 gas particles and 4×256^3 dust particles in all simulations. This was chosen based on the scaling tests in MSH19 (appendix B), which showed reasonable convergence in the mid- k regime between 128^3 and 256^3 (although RDI simulations of this type can never be truly converged because the instability generally grows fastest at the smallest scales of the box).⁴ MSH19 also showed convergence in RDI dust probability-density functions (PDFs) once the dust resolution

⁴ The numerical time step in all simulations is strongly limited by the integration of the smallest grains, which have a very short stopping time. This increases their computational cost by a factor of ≈ 10 compared to an equivalent system without dust, which, combined with the relatively slow saturation of the RDI (up to $t \approx 30L/c_s$), makes the simulations relatively computationally expensive despite their modest resolution.

approached that of the gas (a factor 4 lower gives good results, but not a factor 16 lower) in line with previous works (e.g., Bai & Stone 2010); our choice of 4×256^3 dust particles is made due to the wide range of grain sizes in our simulations and is explored further in App. B. Although we use an MRN dust-mass distribution in all cases $d\mu/d \ln \epsilon_{\text{grain}} \propto \epsilon_{\text{grain}}^{1/2}$, we use an equal number of numerical super-particles randomly sampled across each logarithmic size range (i.e., the super-particles change in their “total” super-particle mass proportionally to $\epsilon_{\text{grain}}^{1/2}$) in order to not under-resolve the small particles. We note that some of the convergence problems that are well known in the numerical computation of polydisperse dust instabilities seem to be less severe in our simulations than in previous works on the protoplanetary disk streaming instability (Krapp et al. 2019; Paardekooper et al. 2021). The difference here may be due to differences between the linear properties of the acoustic RDI and the streaming instability, or could relate to the numerical method, whereby grains are randomly sampled in size space across the full distribution, each with their own stopping time (it is thus effectively a type of Monte-Carlo integration scheme). We investigate this convergence further in App. B by comparing the early phases of GIZMO simulations to linear results; however, in order to understand the influence of both the numerical method and the instability’s properties, further study of these issues would be beneficial.

In the no-backreaction, driven cases, we use time-correlated incompressible (solenoidal) forcing at the largest scales (Fourier modes with $k \leq 4\pi/L$; Hopkins & Lee 2016). The correlation time is $0.5L/c_s$ in the constant-drift simulation and $0.2L/c_s$ in the non-constant-drift simulation, because the turbulence in the non-constant-drift case has higher Mach number, so a shorter box-crossing time. We use the total dust-to-gas-mass ratio $\mu_0 = 0.01$ for both of the RDI simulations ($\mu_0 = 0$ for the no-backreaction simulations).

2.4.2 Grain-size bins for diagnostics

Although our simulations involve a continuous distribution of grain sizes, for most diagnostics – for instance, any quantity involving dust density or velocity as per Eq. (5) – it is necessary to bin the dust size distribution. We choose to do this across 8 logarithmically spaced bins, which we label with $\epsilon_{\text{gr},1}$ for the smallest grains, through to $\epsilon_{\text{gr},8}$ for the largest grains. More precisely, the label $\epsilon_{\text{gr},i}$ refers to grains with ϵ_{grain} between $10^{b_i} \epsilon_{\text{grain}}^{\text{max}}$ and $10^{b_{i+1}} \epsilon_{\text{grain}}^{\text{max}}$, where $b_i = (-2, -1.75, -1.5, -1.25, -1, -0.75, -0.5, -0.25, 0)$. So, for example, grains of size $\epsilon_{\text{gr},1}$ have a density and bulk velocity given by Eq. (5), with $\epsilon_{\text{gr},1} = 10^{-2} \epsilon_{\text{grain}}^{\text{max}} = \epsilon_{\text{grain}}^{\text{min}}$ and $\epsilon_{\text{gr},8} = 10^{-1.75} \epsilon_{\text{grain}}^{\text{max}} \approx 1.78 \epsilon_{\text{grain}}^{\text{min}}$.

2.5 Mapping to astrophysical applications

Our simulations are not intended to map to a specific astrophysical object, but rather study the generic behavior of RDI-generated turbulence. Here, we outline how the simulation units – with $\langle \rho_g \rangle = 1$, $c_s = 1$, $\bar{\rho}_{d,\text{int}} = 1$, and $L = 1$ (the box size) – translate into various astrophysical situations and processes of interest. The two important properties are the grains’ drift velocity – which depends on the radiation field, grain size, and other gas properties – and the physical box scale L_{phys} , which depends on the gas density and grain sizes. Following HS18, we briefly consider as examples asymptotic giant-branch (AGB) stars, Active Galactic Nucleii (AGN), and star-forming regions (giant molecular clouds; GMCs), which are the contexts most relevant to uncharged dust; more detailed esti-

mates for a wider range of situations are given in Hopkins & Squire (2018b) (see their figure 6).

A simulation can be mapped to a given physical situation by comparing the box size $L = 1$ to the grain-drift length at $w_s = 0$, $L_{\text{drift}} = c_s t_s |_{w_s=0} = \sqrt{\pi/8} \epsilon_{\text{grain}} \bar{\rho}_{d,\text{int}} / \rho_g$. In order to obtain the desired w_s and $(2\pi/L)c_s t_s$, as discussed above, the constant-drift simulations use $\epsilon_{\text{grain}}^{\text{max}} = 0.15 = 100 \epsilon_{\text{grain}}^{\text{min}}$, while the non-constant-drift simulations use $\epsilon_{\text{grain}}^{\text{max}} = 0.0878 = 100 \epsilon_{\text{grain}}^{\text{min}}$. Thus, the box scale translates into $L_{\text{phys}} \approx 6.7 \epsilon_{\text{grain}}^{\text{max}} \bar{\rho}_{d,\text{int}} / \rho_g$ and $L_{\text{phys}} = 11.4 \epsilon_{\text{grain}}^{\text{max}} \bar{\rho}_{d,\text{int}} / \rho_g$ for the constant- and non-constant-drift cases, respectively.

Star-forming regions HS18 estimates GMC conditions under reasonable assumptions (e.g., a cloud of $\sim 10\text{pc}$ that has converted ~ 0.1 of its mass into stars), finding $w_s \sim 10$ for larger grains with $Q_{\text{abs}} \sim 1$ (w_s is larger closer to a more luminous source and at lower gas density). Depending on the wavelength of the radiation and the dominant grain sizes, this is in reasonable agreement to both the constant- and non-constant-drift simulations. The above estimates yield $L_{\text{phys}} \approx 20\text{pc}$, showing that the smaller-scale, shorter-time dynamics in our simulations will apply to larger scales around a GMC.

AGB-star winds The envelopes/winds of AGB stars are dust laden and driven by radiation pressure. Using similar estimates to HS18 (a stellar luminosity of $\sim 10^5 M_{\odot}$ with mass-loss rate $\sim 10^{-4} M_{\odot} \text{yr}^{-1}$) yields $w_s \sim 0.1 \rightarrow 10$, which is in the range probed by either simulation. Similarly, estimating the gas density at $\sim 1\text{AU}$ from a star with a wind velocity $\sim 10\text{kms}^{-1}$ yields $L_{\text{phys}} \sim 5 \times 10^{-5} \text{AU}$ showing that our boxes are probing relatively small scales inside the outflowing wind, where the RDI would seed small-scale clumping.

AGN-driven outflows HS18 and Hopkins & Squire (2018b) estimate very fast drift velocities, from $w_s \sim 1$ for small grains to $w_s \gtrsim 100$ for larger grains, in the “dusty torus” region around an AGN with luminosity $\sim 10^{46} \text{ergs}^{-1}$. Using $n \sim 10^6 \text{cm}^{-3}$, as appropriate to a denser closer-in region, yields $L_{\text{phys}} \sim 2 \times 10^{-4} \text{pc}$, showing that (as for the AGB wind), the numerical box represents a small patch of the larger system, representing fast dust dynamics on small scales.

Overall, we see that our simulation parameters are likely most applicable to AGB winds; GMC-related applications would be better served by a somewhat smaller-scale box, while the drift velocities in the AGN are somewhat more extreme than simulated. Also, grain charging and MHD effects are likely more important for many GMC-like conditions, which would change our results substantially (Hopkins et al. 2021). However, parameters in all three cases vary enormously, and the physical ideas we explore are generally relevant to different regions of all three cases. Our chosen dust-to-gas-mass ratio of $\mu_0 = 0.01$ broadly applies to most situations, although this can vary significantly both above and below this value (see, e.g., Knapp 1985; Dharmawardena et al. 2018; Wallström et al. 2019 for some examples of AGB winds).

3 RESULTS

In this section we present results of the four GIZMO simulations outlined above (§ 2.4). We start with a general exploration of the time evolution and turbulence structure (§§ 3.1 and 3.2) then consider more detailed statistics related to dust clumping and collisions in § 3.3.

3.1 General morphology and time evolution

In Figs. 1 and 2 we show three-dimensional visualizations of the turbulence structure and the time evolution of important quantities for the constant-drift simulations. The same is shown for the non-constant-drift simulations in Figs. 3 and 4. In each case, the turbulence structure is illustrated during the instability-growth phase (left-hand panels) and once it saturates nonlinearly (middle panels) for the RDI simulations, and compared to the gas and dust structure of the externally forced runs without dust backreaction (right-hand panels). The bottom panels visualize the smallest and largest grains in the RDI, to compare differences in their structure. The time-evolution panels (Figs. 2 and 4) show how velocity dispersions and drift velocities vary with grain size (left-hand panels; insets show the equilibrium dust parameters) and gas and dust velocity dispersions integrated over all grain sizes (middle and right-hand panels), comparing the RDI cases to the driven-turbulence ones (right-hand panels). These plots illustrate the basic time evolution of the RDI through the linear phase and saturation, and allow simple comparison to the saturated state of driven turbulence.

The early-time growth in the constant- and non-constant-drift cases is rather different and well explained by the linear mode structure in each case. In the constant-drift case, the growth is initially rapid but slows in time, broadly matching the predicted linear growth rates (dotted lines in the middle panel of Fig. 2), which increase monotonically with scale (see Fig. A1). This behavior is expected and discussed in previous works on RDI evolution (Seligman et al. 2019; MSH19); it results from smaller-scale modes growing and saturating nonlinearly more rapidly than large-scale modes, so that the growth of a bulk quantity (such as $\langle u_g^2 \rangle$) is first dominated by the faster smaller scales, then, at later times (once the small-scales saturate), by the slower larger scales. Such evolution is also clearly seen in the morphology in Fig. 1: there is strong clumping of small grains at small scales by $t \approx 5L/c_s$ even though the turbulence is far from full saturation at this point. The structures in the gas and dust, which clearly show the RDI resonant angle ($\theta_k = \cos^{-1}(w_s^{-1}) \approx 48^\circ$) are broadly similar to those that develop in saturation at the box scale (middle panel). We see that the smallest grains exhibit the strongest clumping (note higher-density patches in the bottom panels) and have a modestly higher velocity dispersion in the saturated state. However, it is also clear that large and small grains are undergoing similar dynamics: w_s remains remarkably similar for all grains even as it fluctuates in time (left-hand panel of Fig. 2), and high-density regions of large and small grains are clearly correlated spatially (bottom middle panels of Fig. 1). Thus, as suggested by linear calculations (App. A2), the constant-drift RDI involves different grain sizes interacting with the gas in similar ways, driving resonant modes that cause strong clumping for all sizes concurrently.

The non-constant-drift RDI is more complex, with significant differences between the dynamics of small and large grains. As discussed in detail in App. A3, a number of different linear-instability mechanisms can operate and/or dominate in the non-constant-drift RDI, and this is also true for the chosen scale and parameters of the simulation. In particular, there exists a large-scale parallel mode that resembles a backward-propagating sound wave, which has a similar growth rate to a smaller-scale, more oblique resonant mode that predominantly effects the largest grains (see Fig. A2). In App. B, we test the detailed linear growth of these modes across different scales, showing generally good agreement with linear predictions (see Figs. B1 and B3). The effect of this linear mode structure can be seen in the turbulence morphology that develops, as well

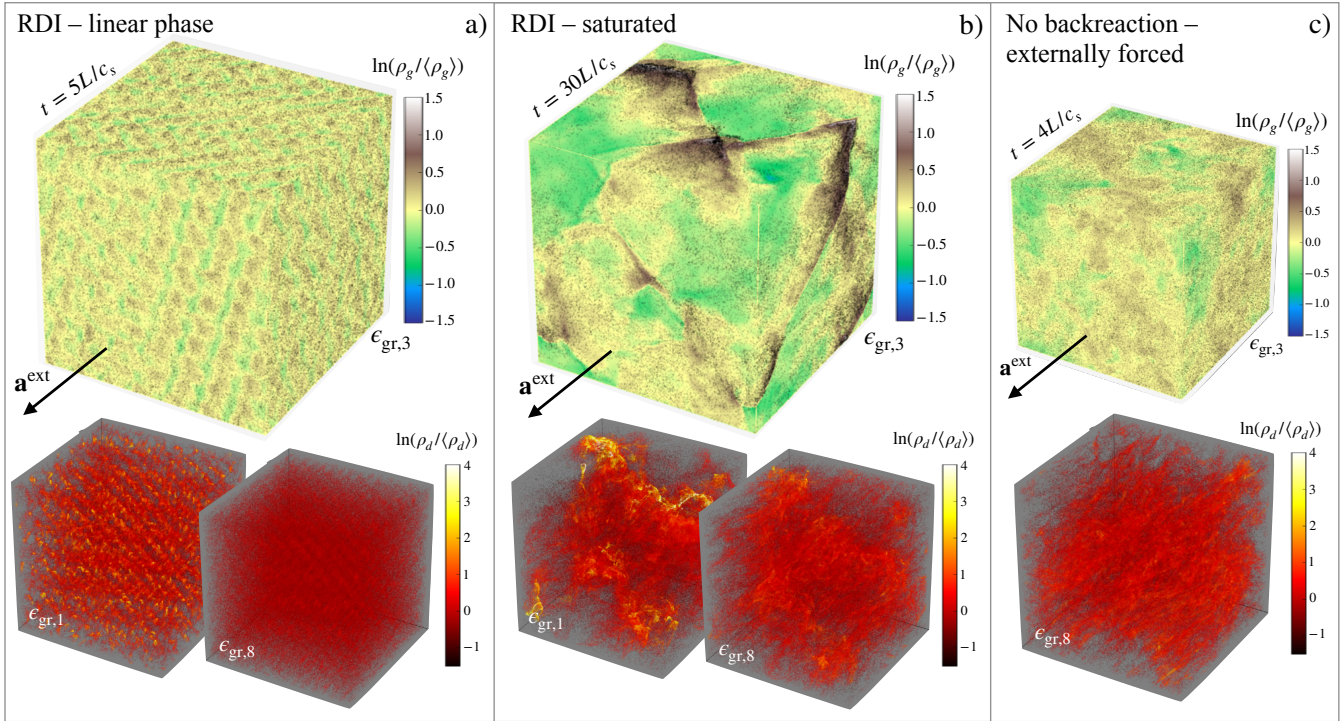


Figure 1. Dust and gas visualizations for the constant-drift simulations. Top images show the gas density on the surface of the cube with medium-sized ($\epsilon_{\text{gr},3}$) grains shown as black dots, while bottom images show volume renderings of the dust density for small ($\epsilon_{\text{gr},1}$) and large ($\epsilon_{\text{gr},8}$) grains (the dust binning is described in § 2.4.2). Panel (a) shows the near-linear phase of the RDI at early times and panel (b) shows its saturated turbulent state at late times (see also Fig. 2). Panel (c) illustrates the saturated turbulence in the no-backreaction constant-drift simulation, where the turbulence is externally forced (only large grains are shown in the bottom image).

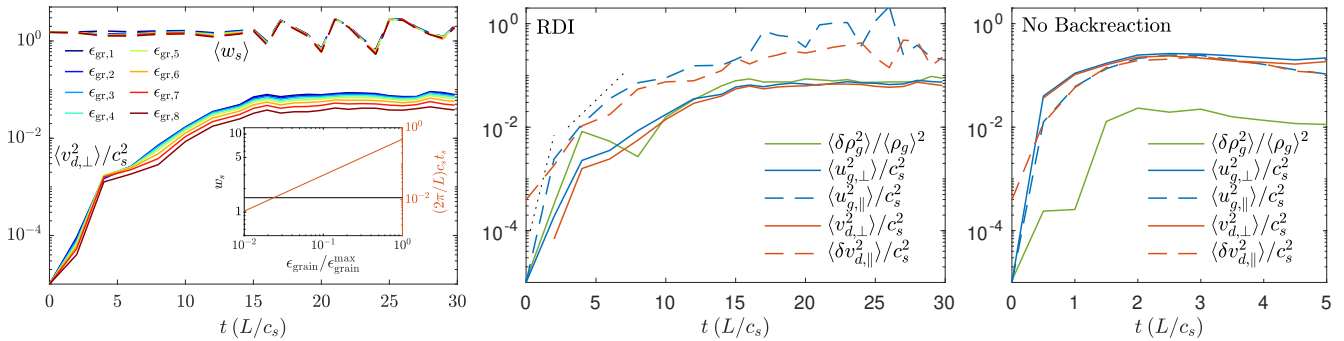


Figure 2. Time evolution of bulk quantities in the constant-drift simulations. The left-hand panel shows the evolution of dust-related quantities in the RDI simulation for different-sized grains from small ($\epsilon_{\text{gr},1}$; blue) to large ($\epsilon_{\text{gr},8}$; red), showing the measured perpendicular dust velocity dispersion $\langle \delta v_{d,\perp}^2 \rangle = \langle v_{d,\perp}^2 \rangle$ with solid lines, and the drift velocity $\langle w_s \rangle = \langle v_{d,\parallel} \rangle$ with dashed lines. The inset shows the equilibrium $w_s(\epsilon_{\text{grain}})$ (black, left axis) and $t_s(\epsilon_{\text{grain}})$ (red, right axis). Similar quantities for the gas and dust averaged over all bins are shown in the middle panel for the RDI simulation, and in the right-hand panel the no-backreaction case with externally driven turbulence. Their comparison shows clear differences in the structure of RDI-driven turbulence (larger parallel velocity fluctuations and stronger relative density fluctuations) that cannot be matched by isotropic incompressible driving. In taking averages, gas quantities are weighted by the gas mass and dust quantities by the dust mass. The black dotted lines in the middle panel show the linear growth rates of resonant modes with $k \approx 32\pi/L$ (approximately 1/16 of the box scale) and $k \approx 2\pi/L$ (approximately the box scale); see Eq. (A11) and Fig. A1.

as in the time evolution of the RDI. We see the formation of a box-scale strong shock at early times (left-hand panel of Fig. 3), which creates a strong density contrast in the gas and the smaller dust grains (because they are better coupled to the gas). It is also clear in the gas and dust time evolution (middle panel of Fig. 4), manifesting as a large density dispersion that develops until $t \approx 5L/c_s$, at which point it breaks up and grows larger turbulent velocity fluctuations

into the true steady state for $t \gtrsim 8L/c_s$. The visual turbulent morphology in the saturated state at late times (middle panel of Fig. 3) is quite different from the driven turbulence (right-hand panel), with smaller-scale structures in the gas caused by highly elongated dust velocity filaments. We interpret this behavior as being due to the quasi-resonant mode, which affects only the largest grains and is highly oblique because of their fast drift velocity

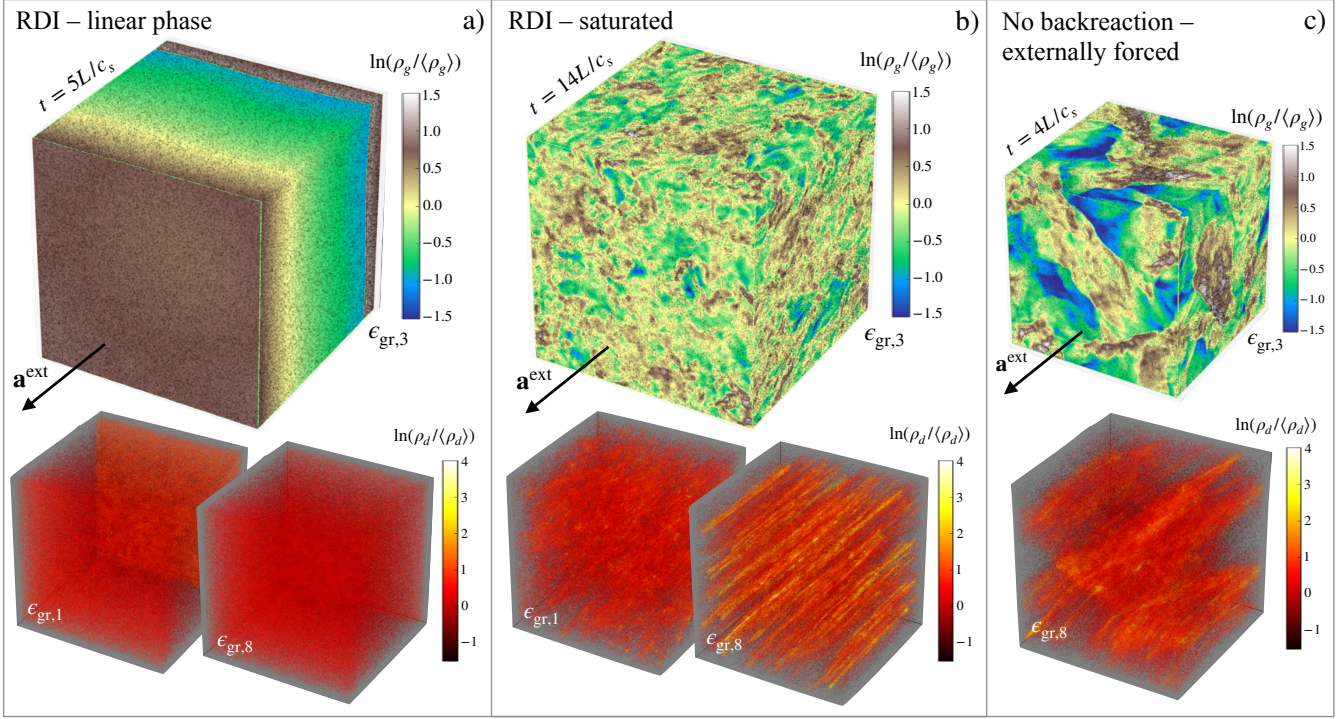


Figure 3. As for Fig. 1, but for the non-constant-drift simulations.

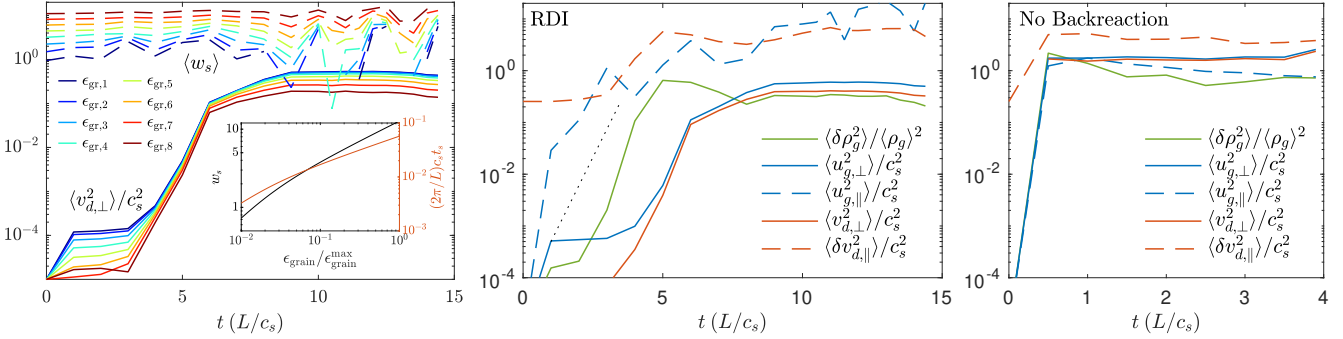


Figure 4. As for Fig. 2, but for the non-constant drift simulation. Because the larger grains, with most of the mass, move faster in this case, the resulting turbulence is trans-sonic, with $\langle u_g^2 \rangle \sim c_s^2$ and larger density fluctuations than the constant-drift simulation. The black dotted line in the middle panel indicates the linear growth rate of the box-scale mode seen in the left panels of Fig. 3; the details and convergence of this linear growth phase are assessed in detail in App. B.

(Fig. A2 inset and Fig. B3); indeed, there is strong, oblique clumping of large grains but not small grains (middle-lower panel). Further evidence for the different dynamics of small and large grains is seen in the evolution of w_s (left-hand panel of Fig. 4), which exhibits much larger fluctuations for small grains than large grains in the saturated turbulence, even though their perpendicular dust velocity dispersions (solid lines) are similar.

3.1.1 The level of turbulent driving

It is worth briefly commenting on some differences between RDI turbulence and the externally forced runs without dust backreaction. The level of forcing in the no-backreaction runs was chosen to match the RDI saturation as best as possible; however, the choice of isotropic forcing in the driven runs means that $u_{g,\perp}^{\text{ms}} \approx 2u_{g,\parallel}^{\text{ms}}$ (where

$u_{g,\cdot}^{\text{ms}} = \langle u_{g,\cdot}^2 \rangle^{1/2}$ is the root-mean-squared gas velocity), while the saturated state of the RDI runs are distinctly non-isotropic, with much larger parallel velocity dispersions $u_{g,\parallel}^{\text{ms}} \gg u_{g,\perp}^{\text{ms}}/2$. Thus, although both RDI cases have a modestly larger total velocity dispersion than their equivalent no-backreaction runs ($u_g^{\text{ms}} \approx 0.9c_s$ versus $u_g^{\text{ms}} \approx 0.6c_s$ for the constant-drift case; $u_g^{\text{ms}} \approx 3.6c_s$ versus $u_g^{\text{ms}} \approx 1.7c_s$ for the non-constant-drift case), their perpendicular velocity dispersions are smaller ($u_{g,\perp}^{\text{ms}} \approx 0.3c_s$ versus $u_{g,\perp}^{\text{ms}} \approx 0.5c_s$ for the constant-drift case; $u_{g,\perp}^{\text{ms}} \approx 0.8c_s$ versus $u_{g,\perp}^{\text{ms}} \approx 1.4c_s$ for the non-constant-drift case). In addition, we see that externally forced turbulence has a somewhat lower density dispersion than RDI turbulence in the constant-drift case, while the opposite is true for the non-constant-drift simulations. While it might be possible to rectify some of these discrepancies using non-isotropic driving, such an exercise would not necessarily be helpful: the differences arise

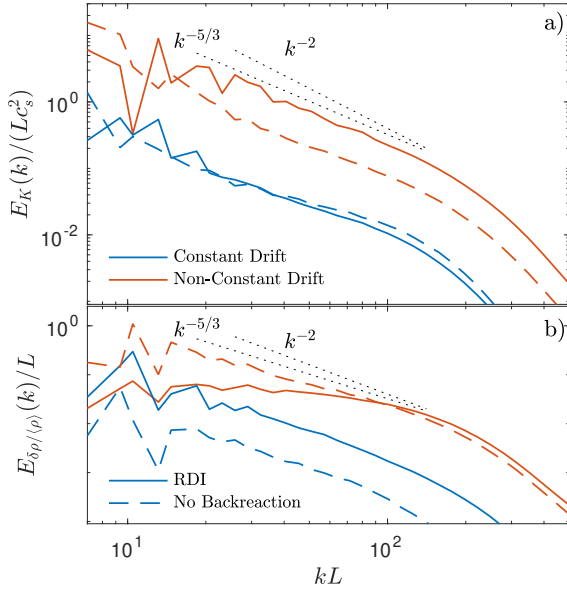


Figure 5. Top panel: gas velocity spectra from all four simulations, with blue lines showing the constant-drift simulations, red lines showing the non-constant-drift simulations, solid lines showing RDI simulations, and dashed lines showing no-backreaction (externally forced) cases. We see similar behavior in all cases, with kinetic energy spectra $\sim k^{-5/3}$ that broadly match previous results for subsonic and trans-sonic turbulence. Bottom panel: gas density spectra, which also broadly match expectations, with a significantly flatter spectrum in the higher-Mach-number non-constant-drift case.

from fundamental differences in the structure and evolution of RDI turbulence and driven turbulence, which is exactly the physics that we wish to study. However, it is important to keep them in mind as we explore some of the differences in more detail.

3.1.2 Turbulent Stokes numbers of grains

A parameter of particular importance for turbulent grain dynamics is the ratio of stopping time to the turnover time of the turbulence, known as the Stokes number, St . For comparison to previous results on dust dynamics in turbulence without backreaction (e.g., Ormel & Cuzzi 2007; Pan & Padoan 2013; Pumir & Wilkinson 2016; Mattsson et al. 2019) it is helpful to estimate St at the largest and smallest resolvable scales in our simulations. The large-scale turnover time is estimated as $\tau_L \sim L/u_g^{\text{rms}}$, which (using the externally forced turbulence values from above to avoid dealing with anisotropic turbulence) is $\tau_L \approx 1.7L/c_s$ for the constant-drift case, and $\tau_L \approx 0.6L/c_s$ for the non-constant-drift case. As expected, the saturation of the turbulent runs, seen in the right-hand panels of Figs. 2 and 4, occurs over a timescale $\sim \tau_L$. The fastest time scale in the turbulence, which occurs at small scales and is termed τ_v , can be estimated from basic Kolmogorov arguments. For a $\sim k^{-5/3}$ velocity spectrum, which is at least roughly valid for the trans-sonic turbulence here (see Fig. 5), the turnover time of structures of lengthscale l scales as $l^{2/3}$. Using twice the average point spacing at our fiducial resolution, $l_v \approx L/128$, as an estimate for the smallest scales available before numerical viscosity starts damping fluid motions, we estimate $\tau_v \approx 0.07L/c_s$ and $\tau_v \approx 0.02L/c_s$ for the constant- and non-constant-drift cases, respectively. Denoting the outer scale and smallest-scale Stokes numbers as $St_L = t_s/\tau_L$ and $St_v = t_s/\tau_v$,

respectively, we thus find

$$St_L \approx 0.01 \left(\frac{\epsilon_{\text{grain}}}{\epsilon_{\text{max}}^{\text{grain}}} \right)^{1/2}, \quad St_v \approx 0.4 \left(\frac{\epsilon_{\text{grain}}}{\epsilon_{\text{max}}^{\text{grain}}} \right)^{1/2}, \quad \text{Non-constant drift,}$$

$$St_L \approx 0.05 \frac{\epsilon_{\text{grain}}}{\epsilon_{\text{max}}^{\text{grain}}}, \quad St_v \approx 1.1 \frac{\epsilon_{\text{grain}}}{\epsilon_{\text{max}}^{\text{grain}}}, \quad \text{Constant drift.} \quad (9)$$

We see that these simple estimates would naively suggest that nearly all grains in our simulations are “well coupled” ($St \lesssim 1$) to the gas turbulence across all scales, meaning that they should passively trace gas motions. We will show below that small grains in the constant-drift RDI are actually not “well coupled” to the gas turbulence in this sense, despite the fact that $St_v \approx 0.01$ for this population. This is likely because the compressive and dust-drift motions associated with the instability are both faster (thus increasing St) and more effective at driving dust clumping. Finally, it is worth noting that the RDI quasi-linear saturation estimate of MSH19, $u_g^{\text{rms}} \sim \mu^{1/2}(c_s t_s/L)^{-1/2}$, which compared well against single-grain-size simulations, yields similar estimates for St ; $St_v \sim \mu^{1/2}(c_s t_s/L)^{1/2}(l_v/L)^{-2/3}$, for the Stokes number on scale l_v , which is generally $\ll 1$ for outer scales in the low- or mid- k regime with $\mu \ll 1$, except at very small scales. Thus, it seems that simple (Kolmogorov) estimates of turbulent Stokes numbers in RDI turbulence generically yield rather small values ($St \ll 1$) compared to what is usually necessary to strongly clump grains in turbulent flows (i.e., $St \gtrsim 1$; see, e.g., Hopkins & Lee (2016), who see only very weak clumping for $St \ll 1$ in compressible turbulence with the same numerical methods).

The discussion above also suggests that another clumping regime could emerge at extremely small scales: at scales where $St_v \gg 1$, the turbulent cascade may start to dominate the clumping for grains that are not strongly affected directly by the RDI. Given the efficiency of the constant-drift RDI at clumping all grain sizes, such an effect would likely be important only for smaller grains in the non-constant-drift regime, and would manifest as an enhanced clumping at larger resolution. Using the estimate (9), we see that accessing this regime – $St_v \gtrsim 1$ for the smallest grains – requires St_v to be ≈ 100 times larger than the simulations presented here, thus requiring ≈ 1000 times more resolution elements in each direction (assuming $\tau_v \propto l^{2/3}$). This is clearly unattainable with present resources, although it is possible that a similar regime could be accessed with a different set up.

3.2 The turbulent steady state

In this and the following section, we explore more detailed statistics of the saturated states of RDI turbulence, comparing to the turbulence runs as a reference.

Spectra The simplest measure of the scale-dependent turbulent structure is the spectrum, which is illustrated for all four cases in Fig. 5. The kinetic energy spectra (panel a) of RDI turbulence and externally forced (no-backreaction) turbulence are seen to be quite similar. Spectral slopes in the inertial range ($20/L \lesssim k \lesssim 200/L$) are approximately $\sim k^{-5/3}$, as expected for a standard Kolmogorov cascade, and are slightly steeper in the non-constant-drift runs, as expected because of their higher Mach numbers (velocity spectra steepen to $\sim k^{-2}$ for highly supersonic flows; e.g., Federrath 2013). The consistency of the RDI and forced velocity spectra is interesting, given the clear differences in their structures observed in Figs. 1 and 3. For example, we see that although the non-constant-drift RDI turbulence looks quite different to its forced counterpart,

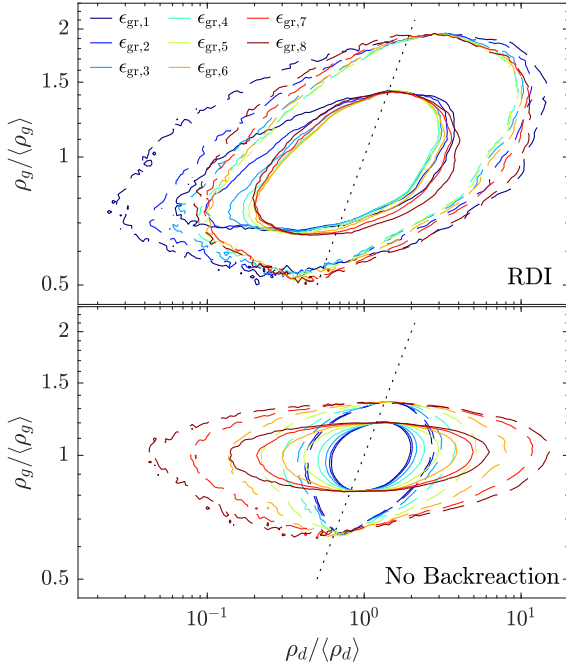


Figure 6. Two-dimensional volume-weighted PDF of the local (resolution-scale) dust density $\rho_d(\epsilon_{\text{grain}})$ and gas density ρ_g for the constant-drift simulations. Solid lines show contours at 0.1 of the maximum, while dashed lines show the contour of 0.01 of the maximum, with each color showing the PDF for different grain-size bins from the smallest grains $\epsilon_{gr,1}$ in blue, to the largest $\epsilon_{gr,8}$ in dark red. The PDFs are averaged over 3 snapshots during the saturated phase. The two cases are markedly different: in externally forced turbulence case without backreaction (bottom panel) the smallest grains mostly trace the gas and larger grains exhibit more clumping; in the RDI turbulence, the smallest grains instead exhibit the strongest clumping, with a long tail extending to very small dust densities.

with smaller-scale features, the scaling of the spectra at smaller wavenumbers $k \geq 20/L$ is very similar. The density spectra (panel b) are also consistent with previous works (Konstandin et al. 2016), although we see more interesting differences between the RDI and externally forced turbulence runs. The constant-drift runs exhibit similar, relatively steep ($\sim k^{-2}$) spectral scaling, but with stronger compressive motions in the RDI (see also Fig. 2); however, the non-constant-drift density spectra are quite different, perhaps because of the higher-mach-number parallel flows in the RDI case.

Dust and gas distribution A useful measure of the level and structure of dust clumping is the joint Probability Density Functions (PDFs) of dust and gas density, the contours of which are shown in Figs. 6 and 7 for the constant- and non-constant-drift cases, respectively. These illustrate how regions of high gas density correlate with those of high dust density, and likewise for low-density regions. The black dotted lines illustrate the one-to-one correlation that would be observed if dust were perfectly coupled to the gas.

Let us first consider the constant-drift case (Fig. 6), which shows a significant difference between the RDI-generated turbulence (top panel) and the forced turbulence without dust backreaction (bottom panel). This is surprising, given the similarity of their spectra. Most clearly, we see that in RDI turbulence the smallest grains (blue contours) exhibit larger fluctuations than the larger grains (red contours), particularly at low-densities, in stark contrast to the no-backreaction runs. The characteristic shape – with a high-

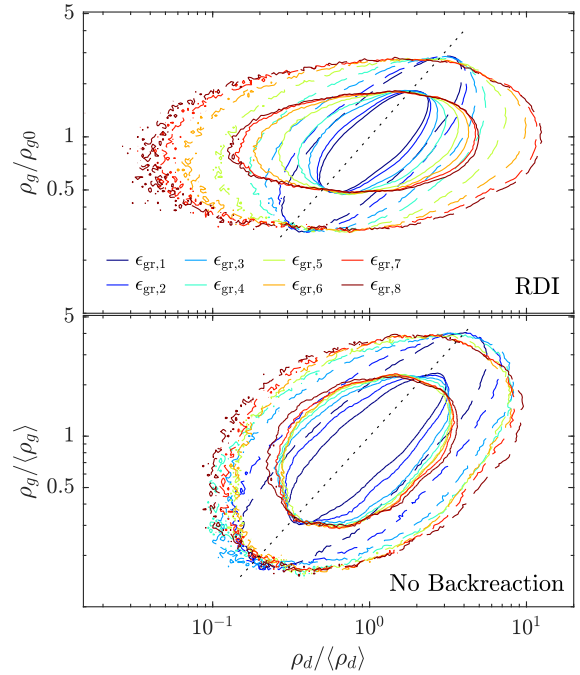


Figure 7. Same as Fig. 6, but for the non-constant-drift simulation. The RDI PDF is more similar to externally forced turbulence in this case, although we still see significantly wider dust-density distributions (despite the somewhat narrower gas-density distribution), particularly for the largest grains that are more strongly affected by the mid- k RDI (see text).

probability of low dust density in lower-gas-density regions – was also seen in MSH19 and seems to be a typical feature of the saturated state of the mid- k (or high- k) RDI. The much wider dust density distribution of larger grains in externally forced turbulence is well explained by their relative turbulent Stokes numbers (which are quite small across all scales for the smallest grains; see §3.1.2, Pan & Padoan 2013; Hopkins & Lee 2016; Mattsson et al. 2019), so the fact that this is not true for the RDI turbulence is an important illustration of its different grain-clumping mechanisms.

In contrast, the non-constant-drift RDI PDFs appear more similar to externally forced turbulence (Fig. 7), although the dust-density distribution is wider for the larger grains in the RDI case (i.e., the difference between the large and small grains is larger). This is likely because the highly oblique resonant instability, which is driven only by the large grains (see middle panel of Fig. 3), is particularly efficient at grain clumping; the backward-propagating sound-wave mode, in contrast, clumps grains in a similar way to standard turbulence, creating a similar (small) density dispersion in the smaller grains. This explanation is commensurate with the enhanced clumping of all grains (compared to driven turbulence) in the constant-drift case, where the resonant instability operates with all grain sizes.

3.3 Dust clumping and collisions

The observations above, along with previous results (MSH19; Seligman et al. 2019; Hopkins et al. 2020), show that the grain-clumping and its dependence on grain size can be very different in the RDI compared to externally forced turbulence without backreaction. The most obvious question that arises is whether these differences significantly change grain-collision statistics in the RDI

compared to previous theories (Voelk et al. 1980; Zaichik et al. 2006; Pan & Padoan 2013; Mattsson et al. 2019; Li & Mattsson 2020). Two key properties influence grain collisions and are needed to compute the collision kernel: the first is the relative clumping of grains in space (Maxey 1987), the second is the relative velocity of grains that do collide (e.g., Pumir & Wilkinson 2016). Put together, these can be used to construct estimates for the collision rate and the sticking-bouncing-fragmentation probabilities (e.g. Garaud et al. 2013; Pan et al. 2014b), an understanding of which is key for estimating how turbulence influences grain growth in astrophysical scenarios (e.g., in an AGB outflow). A full, careful estimate of these probabilities requires grappling with a number of subtle convergence issues; for instance, relative grain velocities depend on particle separation, and estimating the true collision velocity (at near-zero particle separation) requires a careful consideration of how different physical effects contribute to the relative velocity (Falkovich et al. 2002) and how these are affected by numerics (Pan & Padoan 2014; Haugen et al. 2021). Our goal here is less detailed – to compare and contrast the relative clumping and grain-collision velocities between the constant- and non-constant-drift RDIs and externally forced turbulence without dust backreaction. We find much stronger clumping and reduced collision velocities of grains in the constant-drift RDI, with qualitatively different trends for small grains and grains of different sizes. These trends are sufficiently strong to reveal clear differences between grain-grain collisions in the RDI and externally forced turbulence. We thus forgo a careful study of the convergence to the zero-particle-separation limit, which would be a formidable task for RDI turbulence given the wide range of different regimes (Hopkins & Squire 2018a). Overall, our results suggest that the RDI could strongly enhance grain growth rates in outflows, especially in the constant-drift regime ($\epsilon_{\text{grain}} \gg \lambda_{\text{rad}}$).

3.3.1 Grain clumping

The key measure of relative grain clumping is the Radial Distribution Function (RDF), $g(r; \epsilon_{\text{gr},l}, \epsilon_{\text{gr},h})$, which measures the relative probability of finding a grain of size $\epsilon_{\text{gr},l}$ a distance r from a grain of size $\epsilon_{\text{gr},h}$. It is normalized such that a spatially homogeneous distribution satisfies $g(r; \epsilon_{\text{gr},l}, \epsilon_{\text{gr},h}) = 1$. If $g(r; \epsilon_{\text{gr},l}, \epsilon_{\text{gr},h}) > 1$ for small r , the collision rate of $\epsilon_{\text{gr},l}$ grains with $\epsilon_{\text{gr},h}$ grains will be enhanced compared if their distribution were uncorrelated (Maxey 1987; Squires & Eaton 1990). As well as grain collisions, a highly clumped grain distribution could have interesting implications for the opacity, which may be significantly reduced compared to a homogenous grain distribution if photons are primarily scattered around the low-density regions between dust clumps (see Steinwandel et al. 2021).

We illustrate the RDF for the constant- and non-constant-drift simulations in Figs. 8 and 9, comparing the RDI and no-backreaction forced simulations in the top and bottom panels, respectively. We represent g using the same method as Pan & Padoan (2014), setting $\epsilon_{\text{gr},l} < \epsilon_{\text{gr},h}$ and plotting $g(r; \epsilon_{\text{gr},l}, \epsilon_{\text{gr},h})$ as a function of $\epsilon_{\text{gr},h}$ for a variety of grain-size ratios $\epsilon_{\text{gr},h}/\epsilon_{\text{gr},l}$. Grains are binned before computing g according to the method of § 2.4.2. The different line styles show different r , which are computed by including only those grains that lie a distance $r \pm \Delta r$ from each other⁵; the solid lines show $r = L/256$ (the equilibrium gas-particle spacing) and

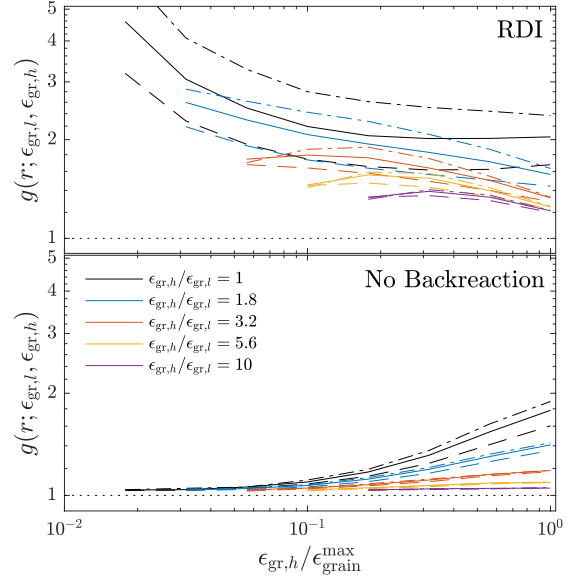


Figure 8. Grain-grain density correlation functions $g(r; \epsilon_{\text{gr},l}, \epsilon_{\text{gr},h})$ for the constant-drift simulations as a function of the “primary” (larger) grain size $\epsilon_{\text{gr},h}$, using the 8 grain-size bins of § 2.4.2. This measures the probability of finding another grain of size $\epsilon_{\text{gr},l}$ a distance r from the primary grain of size $\epsilon_{\text{gr},h}$; i.e., it quantifies the mean local density enhancement between grain pairs. Different line colors show different grain-size ratios $\epsilon_{\text{gr},h}/\epsilon_{\text{gr},l}$, as labeled. Different line styles show the correlation at different particle separations r ; $r = 1/256$ (solid lines), $r = 1/512$ (dot-dashed lines), and $r = 1/128$ (dashed lines; see text for further information). We see much stronger correlations between grains of all sizes in the RDI simulation, with g rising, rather than falling, with decreasing grain size for similarly sized grains. The correlations also rise more rapidly as r decreases in the RDI case, suggesting that the clumping will be even stronger in the $r \rightarrow 0$ limit relevant for grain-grain collisions.

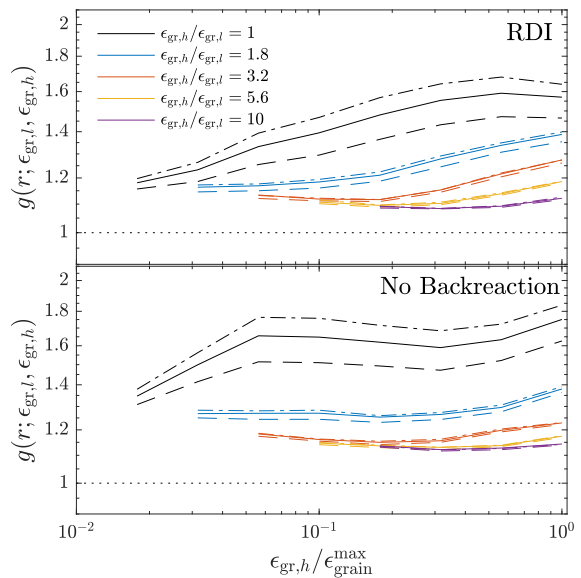


Figure 9. As for Fig. 8, but for the non-constant-drift simulations. The two cases are much more similar than the constant-drift cases, although there remains a modestly higher correlation between larger grains of different sizes in the RDI turbulence.

⁵ The turbulence itself is anisotropic with respect to the drift direction, meaning that g can differ depending on whether r is in the perpendicular

$\Delta r = L/1024$, the dashed lines show $r = L/128$ and $\Delta r = L/4096$, and the dot-dashed lines show $r = L/512$ and $\Delta r = L/1024$ (note that a relatively wider bin in r is needed when r itself is smaller in order to obtain sufficient particle statistics). Let us first consider the externally forced turbulence constant-drift case, since this is most directly comparable to previous work, broadly following the expected behavior (c.f. figure 1 of Pan & Padoan 2014). The strongest turbulent clumping is seen for the largest grains, which is consistent with the well-documented observation that clumping is strongest for particles with $St_v \approx 1$ (Squires & Eaton 1990; Sundaram & Collins 1997) and the estimate in Eq. (9) that all particles have $St_v \lesssim 1$. The maximum of $g \approx 2$ is less than some previous works, and it is also clear from the trend that larger grains would clump more strongly. There are a number of possible causes for this discrepancy: in our driven-turbulence simulations the grains are streaming through the turbulence (unlike previous studies, which used $a^{\text{ext}} = 0$), which could interfere with the “sling” effect that causes turbulent clustering; or the effective viscous scales could be underestimated in the estimates of §3.1.2, thus overestimating St_v ⁶; or, by not including explicit viscosity, we may not be accurately simulating the sub-viscous-scale flows that determine the clumping of the $St_v \approx 1$ grains. The decrease in clumping between different-sized particles (compared to particles of the same size) is similar to that shown in Pan & Padoan (2014).

The constant-drift RDI contrasts significantly to the externally forced turbulence. Most obviously, there is much higher clumping for all grain sizes, but particularly for the smallest grains and in the relative correlations between grains of different sizes. This strong clumping of small grains is notable given that our simple estimates suggested they have very small Stokes numbers ($St \lesssim 0.01$; c.f. driven case in Fig. 8). We also see that our measurements are far from converged, meaning that grains are increasingly clumped at smaller scales, even at scales well below the gas-particle spacing, strongly suggesting that higher-resolution simulations (or reality) would increase g further. Finally, it is worth noting that the general shape of $g(r; \epsilon_{gr,l}, \epsilon_{gr,h})$ with $\epsilon_{gr,h}$ is quite different to those seen in standard hydro turbulence; at least with $\epsilon_{gr,l} \approx \epsilon_{gr,h}$, g becomes independent of ϵ_{grain} for larger ϵ_{grain} , rather than decreasing towards $g = 1$ at either small or large ϵ_{grain} .

The comparison of the non-constant-drift simulations (Fig. 9) tells a less interesting story, showing broadly similar grain distributions between the RDI and externally forced turbulence, and less clumping than the constant-drift RDI. This is consistent with only the largest grains driving interesting dynamics in the non-constant-drift RDI, while the smaller grains are primarily passively advected by the flow. The rather low values of g in these cases are likely related to the fact that all grains have a slightly different equilibrium streaming velocity w_s , meaning that small-scale clumps can be quickly destroyed by grains streaming away from each other (this is discussed further below). The convergence to $g \approx 1.1$, rather than $g = 1$, is simply because the gas is compressible in these simulations, so that there are always some spatial correlations between grains of different sizes that arise due to their mutual correlation with the gas density (see Fig. 7).

or parallel direction. However, we saw only minor differences, when taking this into account, so show only the isotropic version here.

⁶ This is supported by examination of the spectra in Fig. 5: the velocity spectrum steepens at $k \approx 150/L \approx 24(2\pi/L)$, which is well above the scale of twice the gas particle spacing as used in the estimates of Eq. (9).

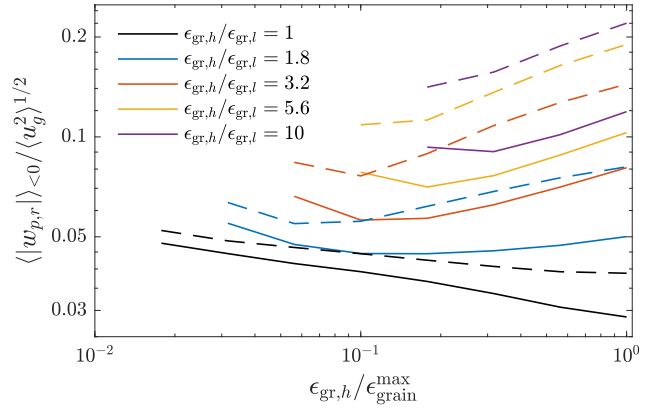


Figure 10. Average collision velocity between grain pairs, normalized by the gas velocity dispersion, in the constant-drift simulations. Solid lines show RDI turbulence and dashed lines show the externally forced turbulence simulation without backreaction (colors show grain-size ratios, as in Fig. 8). We see significantly lower collision velocities in RDI turbulence, particularly between grains of different sizes. Coupled with the larger grain clumping factors in RDI-generated turbulence (Figs. 6 and 8), this would significantly enhance grain coagulation compared to standard estimates.

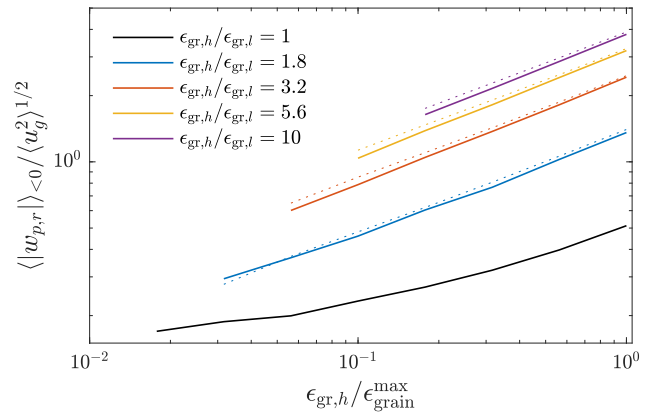


Figure 11. Average collision velocity between grain pairs, normalized by the gas velocity dispersion, in the non-constant-drift RDI simulation (solid lines). The dotted lines show the simple prediction Eq. (10). In this case, the collision velocities are entirely dominated by the different drift velocities of differently sized grains, and the driven and RDI cases look very similar.

3.3.2 Relative velocities

The second component that is required to estimate the rate and outcome of grain-grain collisions is the relative collision velocity. Depending on subtle choices related to the definition of the collision kernel, there are a number of relevant measures of collision velocities that can give slightly different results (Wang et al. 2000; Pan & Padoan 2014). We measure the mean of the value of the radial velocity with which particle pairs approach each other, which is needed to compute the “spherical formulation” of the collision kernel (unlike, for example, the root-mean-squared relative velocity; Wang et al. 2000). More precisely, for two particles with velocities \mathbf{v}_1 and \mathbf{v}_2 and separation vector \mathbf{r} , we define $\mathbf{w}_p = \mathbf{v}_2 - \mathbf{v}_1$ and $w_{p,r} = (\mathbf{v}_2 - \mathbf{v}_1) \cdot \mathbf{r} / |\mathbf{r}|$ and take an average $\langle |w_{p,r}| \rangle_{<0>}$ over only those pairs that are approaching each other. As for the particle RDFs, we plot this separately for different ratios of grain sizes, viz., mea-

sure the collision velocities of large and small particles, as well as those of similarly sized particles. Collision velocity statistics also depend on, and are unconverged in, the particle separation r (i.e., $\langle |w_{p,r}| \rangle_{<0} = \langle |w_{p,r}(r; \epsilon_{gr,l}, \epsilon_{gr,h})| \rangle_{<0}$; Pan & Padoan 2014). By default we use $r = L/256$ (solid lines in Figs. 8 and 9) and comment on this where appropriate. As for the RDFs, the collision velocity statistics are not isotropic in either w_p or r (in either the RDI or the no-backreaction cases); however, examination of anisotropy of collisions has not yielded any interesting insights, so we show only the isotropic versions here.

The constant-drift simulations are shown in Fig. 10. In this case all grains drift at the same average speed, so there is no direct contribution to the collision velocity from the grain’s equilibrium drift velocity. We normalize to gas root-mean-squared velocity in order to make the comparison of the RDI to driven turbulence as apt as possible (see §3.1.1). Overall, we see a modestly lower collision velocity in the RDI for similar sized grains, but the difference becomes more significant for collisions between grains of different sizes. In other words, collisions between large and small grains are significantly slower on average in RDI turbulence compared to standard externally forced turbulence. While this might have been anticipated based on our intuitive understanding that the constant-drift RDI involves gas motions driven by a wide range of dust grains at once, it could have interesting implications for the outcome of grain collisions, for instance, by increasing the size to which grains can grow by sticking (Blum 2018). Finally, it is worth noting that the collision velocities depend relatively strongly on the particle separation r , but this dependence is similar for the RDI and externally forced turbulence so we do not consider it in detail here (see Pan et al. 2014a for extensive discussion).

The non-constant-drift simulations, which are less interesting, are shown in Fig. 11. In these cases, $w_s \sim \epsilon_{\text{grain}}^{1/2}$ is different for each grain size and dominates over the turbulent dust velocity dispersion (see Fig. 4). Grains of different sizes thus collide primarily due to their differing drift velocities, with

$$w_p = v_2 - v_1 \approx [w_s(\epsilon_{gr,2}) - w_s(\epsilon_{gr,1})]\hat{z}. \quad (10)$$

For this reason, unrelated to properties of the turbulence, the RDI and externally forced turbulence simulations produce nearly identical $\langle |w_{p,r}| \rangle_{<0}$ and we plot only the RDI case in Fig. 11. The results match the estimate Eq. (10) nearly perfectly (dotted lines; there is an extra geometric factor of 1/2 because only the radial velocity component is computed). While this is not surprising, it is nonetheless a potentially relevant physical effect that will significantly enhance the collision rate and velocities of grains in outflowing winds in the non-constant-drift regime.

In addition to the mean collision velocities, the PDF of w_p is of interest: rare events can have an important impact on the growth or destruction of grains, for example, by allowing a population to grow beyond particularly important size scales (Garaud et al. 2013; Pan et al. 2014b). We show the PDF of $|w_p|$, $\mathcal{P}(|w_p|; \epsilon_{gr,l}, \epsilon_{gr,h}; r)$ for a variety of grain-size pairs in Fig. 12, illustrating their similar shapes in the RDI and externally forced turbulence for the constant-drift regime.⁷ Given their clear differences in small-scale structure and clumping mechanisms (e.g., Fig. 8) this is surprising. One minor difference is a slightly steeper high- w_p tail (and a slightly flatter low- w_p tail) in the RDI (see light-blue and yellow curves), indicating that high-velocity collisions between differently sized particles

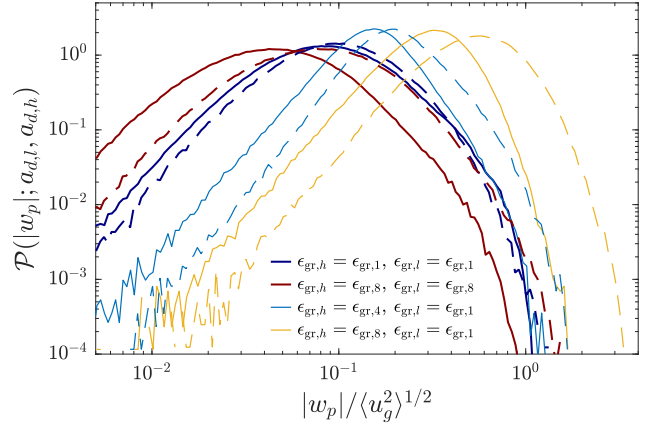


Figure 12. PDF of grain collision velocities $|w_p|$, at particle separation $r = L/256$, for a selection of different grain size pairs in the constant-drift simulations. Solid lines show the RDI, dashed lines show the forced turbulence simulation (see also Fig. 10).

are even less likely than suggested by the collision-velocity average in Fig. 10. However, this seems to be a relatively minor effect.

3.3.3 The collision rate

The collision rate between grains of size $\epsilon_{gr,i}$ and $\epsilon_{gr,j}$ is given by $v_{c,ij} = \langle n_{d,i} \rangle \langle n_{d,j} \rangle \Gamma_{ij}$, where $\langle n_{d,i} \rangle$ is the number density of species i and Γ_{ij} is the collision kernel between i and j . Using the “spherical formulation”,⁸ $\Gamma_{ij} = 2\pi d^2 g(d; \epsilon_{gr,i}, \epsilon_{gr,j}) \langle |w_{p,r}(d; \epsilon_{gr,i}, \epsilon_{gr,j})| \rangle_{<0}$, where d is sum of the radii of the grains. This shows that v_c and/or Γ_{ij} may be inferred (aside from the d dependence) from Figs. 8 to 10. We see that in the non-constant-drift RDI, v_c is large and strongly dominated by the effect of the mean drift; this situation will involve a large number of very high velocity collisions between grains of different sizes. In contrast, the constant-drift RDI collision rate is larger than that of externally forced turbulence for similarly sized grains (by a factor ≥ 4 for small grains), and similar for differently sized grains (since the larger g cancels with the smaller $\langle |w_{p,r}| \rangle_{<0}$). However, the RDI collision velocity is significantly smaller, increasing the probability of slow collisions that lead to grain growth as opposed to bouncing, cratering, or fragmentation.

3.4 Discussion: extensions, limitations, and future work

The parameter space of possible RDIs is very large (Hopkins et al. 2020) and a key limitation of our study has been the focus on just two parameter sets of the acoustic RDI for simulation. That said, for the RDI with neutral gas and grains (acoustic RDI turbulence), most of the likely dependencies on other parameters can be inferred from the results here and those of MSH19. For larger effective scales (smaller $(2\pi/L)c_s t_s$), the linear results in App. A3.1 show that the size distribution of grains becomes unimportant to the instability, suggesting that the non-constant-drift and constant-drift instabilities will both behave similarly to the larger scales of the non-constant-drift simulation presented here, or similar cases

⁷ The non-constant-drift PDFs are dominated by the mean drift velocities, so we do not show them here.

⁸ The alternative “cylindrical” formulation gives very similar results in turbulence simulations, but we have not considered it here (Wang et al. 2000; Pan & Padoan 2014).

in MSH19. For smaller effective scales (larger $(2\pi/L)c_s t_s$), the constant-drift cases will likely behave similarly but with stronger relative clumping for less virulent gas turbulence (MSH19), while the non-constant-drift cases will be limited to less virulent quasi-resonant modes involving only the larger grains (App. A3.2). At smaller dust-to-gas-mass ratio, the results of MSH19 suggest that the gas turbulence will become less virulent, but likely cause more relative dust clumping (the non-constant-drift RDI will also be less virulent at smaller μ , with the resonant instability limited to a smaller range of the largest grains; App. A3.2). At larger dust-to-gas-mass ratio, there is no qualitative change to main features the acoustic RDI (as occurs for the streaming instability; Youdin & Goodman 2005; Squire & Hopkins 2020); rather, the larger mass of the dust simply drives stronger gas turbulence (MSH19). Finally, it is also worth mentioning that while GIZMO seems to be able to capture the linear growth rates of the polydisperse acoustic RDI relatively accurately (see, e.g., Fig. B3), exploring the detailed convergence to linear predictions in different regimes with different grain-size distributions is a complex task beyond the scope of this work (see, e.g., Paardekooper et al. 2021; Zhu & Yang 2021). While unlikely to affect our results here, given the dominance of the large-scale modes in the non-constant-drift simulation, there may be important effects at smaller scales and/or smaller μ , and a more detailed study of numerical convergence and/or comparison to other codes would be important for exploring such cases.

We have also not studied in detail the (likely common) situation where the spectrum of dust grains covers both the constant- and non-constant-drift regimes. Based on linear calculations (see App. A), it is reasonable to surmise that this will behave like the constant-drift RDI for the relevant range of grains (albeit with a somewhat reduced dust-to-gas-mass ratio).

A rather technical source of uncertainty in our results relating to dust-dust collisions concerns the approach to the zero-particle-separation limit. As discussed extensively in Pan & Padoan (2013, 2014); Haugen et al. (2021), a quantitative measurement of the collision kernel requires a careful convergence study in particle separation, which is not achieved here (e.g., compare the different line styles in Fig. 8). This must take into account both explicit dissipative effects, which damp gas motions at small scales, and the different physical contributions to relative grain-grain velocities.⁹ This is well beyond the scope of this work and likely a difficult task for realistic application to astrophysical objects with RDI-generated turbulence. In particular, as well as a better theoretical framework with which to understand the strong clumping even at small Stokes numbers, the acoustic RDI effectively forces the turbulence down to the viscous scales, changing in character with scale. These issues make it difficult to apply Stokes-number-based self-similarity arguments, as usually applied to understand passive grains in turbulence. Thus, the result that constant-drift RDI turbulence should be particularly a effective nursery for grain growth is qualitative at this stage, and we refrain from making quantitative estimates for the collision kernel.

That said, the most relevant and important uncertainty of our study is our neglect of grain charge and gas magnetization. The

⁹ Wilkinson et al. (2006) introduced the decomposition of the grain-grain collision rate into its continuous and “caustic” parts, where the caustic part accounts for collisions that result from grains being slung out from neighbouring eddies. In order to separate these contributions, which is needed to estimate the collision rate in the zero-particle-separation limit, one needs a reasonable model for the behavior of a grain in a representative turbulent eddy (Pan & Padoan 2013; Pumir & Wilkinson 2016).

neutral cases explored here provide a reasonable approximation for cooler, denser regions, for instance around AGB stars, or in some parts of the cool ISM; but, in most astrophysical scenarios where RDIs apply, grain charge and gas magnetization are expected to play a key role. Further, magnetized-RDI turbulence causes significantly stronger clumping than acoustic-RDI turbulence, even in the regime where drag forces are stronger than Lorentz forces and/or in the non-constant-drift regime.¹⁰ A selection of cases is presented in Hopkins et al. (2021), mostly focusing on the more complex situation of a stratified wind driven from the base: extremely strong clumping is seen even in non-constant-drift cases (their “-Q” simulations; see e.g., their figure 9) in stark contrast to our results here, a difference that is related to the magnetization and not the stratification of the system (see e.g., their figure 13; this is also seen in unstratified magnetized simulations). From these results it is clear that magnetization will be a key parameter for RDI-turbulence induced grain clumping; however, given the complexity of these cases and the yet wider parameter space to explore, we leave such studies to future work.

Finally, it is worth mentioning that by neglecting explicit stratification of the system, we are also neglecting other possible gas and/or radiative instabilities that can occur in dust-driven winds for some systems (see, e.g., Woitke 2006; Krumholz & Thompson 2012). Generically, such instabilities operate on much larger scales than the acoustic RDIs considered here, although it is plausible that they could create turbulence that influences RDI development in some circumstances. Again, such issues are addressed more explicitly in the stratified simulations of Hopkins et al. (2021).

4 CONCLUSIONS

This paper has presented an in-depth study of the “acoustic Resonant Drag Instability” (Squire & Hopkins 2018a; HS18), which is driven by the interaction of an outflowing population of dust grains with compressible gas motions. The acoustic RDI is expected to operate in a variety of astrophysical scenarios, for example, in the presence of a radiation source that couples more strongly to dust grains than to the gas. This accelerates grains outwards, often to supersonic velocities, which (in addition to driving a gas outflow) destabilizes the RDI (HS18). In cooler, denser gas, such as that in molecular clouds, AGB-star winds, or around AGN, the grain charge and MHD effects are not necessarily dominant, and the system may be well approximated by considering a neutral gas and neutral grains (the “acoustic” RDI). The novel feature of this work has been the inclusion of a wide spectrum of grain sizes – a factor of 100 in grain radius ϵ_{grain} in our numerical simulations – which has not been included in previous studies but is clearly an important feature of realistic systems (Draine 2010). In our numerical study, rather than surveying a wide parameter space of different simulations, we have focused in detail on two representative cases that can apply adequately well to a variety of astrophysical processes. By comparing directly to simulations of externally forced turbulence, this allowed us to consider in more detail aspects of dust and gas structure in the RDI, and how these might influence important processes such as grain growth.

With a spectrum of grains, there are two qualitatively different regimes of the RDI depending on how the grain’s acceleration

¹⁰ It remains unclear exactly why this is, although there are many more resonant instabilities available in the magnetic case due to the wider variety of waves and the dust’s gyromotion.

(imparted, for example, by an external radiation field) scales with the grain radius. In the *constant-drift* regime, applicable for grains larger than the wavelength of a radiation field ($\epsilon_{\text{grain}} \gtrsim \lambda_{\text{rad}}$), all grains drift through the gas with the same velocity in the (quasi-)equilibrium. In the *non-constant-drift* regime, applicable for small grains in long-wavelength radiation fields ($\epsilon_{\text{grain}} \lesssim \lambda_{\text{rad}}$), or when the acceleration difference between the dust and gas arises from an external force on the gas, the grain drift velocity increases with grain size, stretching across a wide range of values in realistic scenarios.

We show in App. A, which presents analytic and numerical calculations of the linear RDI growth rate with a spectrum of grains, that these different regimes strongly influence the behavior of the acoustic RDI. Generally, the RDI is more virulent, with faster growth rates and behavior that is very similar to the single-grain-size case, in the constant-drift regime. Our simulations show that this linear behavior carries over into the nonlinearly turbulent regime also: the non-constant-drift RDI, although strongly unstable with a saturated state that shares key features of the linear instability, develops into turbulence without strong correlations between grains of different size (like externally forced turbulence); the constant-drift RDI is very different, with much stronger spatial correlations between small grains and those of different sizes, along with slower grain-grain collision velocities. These differences, which imply a high rate of low-velocity collisions in the constant-drift RDI, suggest that constant-dust-drift outflows could be highly effective sites for dust growth through collisions, while the opposite is likely true in the non-constant-drift regime because grain-grain collisions are dominated by the (fast) mean drift between grains of different sizes. Another interesting conclusion in the constant-drift regime is the strong clumping of small grains, even though their turbulent Stokes numbers remain well below one (see §3.1.2). This highlights the fact that the clumping mechanism in RDI-generated turbulence is quite different – and much more efficient for similar velocity dispersions – to standard (Kolmogorov) turbulence (Pumir & Wilkinson 2016), even though the turbulent velocity spectra are relatively similar (Fig. 5).

ACKNOWLEDGMENTS

We thank Eric Moseley and Darryl Seligman for helpful discussion. Support for JS was provided by Rutherford Discovery Fellowship RDF-U001804 and Marsden Fund grant UOO1727, which are managed through the Royal Society Te Apārangi. Support for JS, PFH, and SM was provided by NSF Collaborative Research Grants 1715847 & 1911233, NSF CAREER grant 1455342, and NASA grants 80NSSC18K0562 and JPL 1589742. Numerical simulations were run on the Caltech compute cluster “Wheeler,” and with allocation TG-AST130039 from the Extreme Science and Engineering Discovery Environment (XSEDE), which is supported by National Science Foundation grant number ACI-1548562.

Data availability The simulation data presented in this article is available on request to JS. A public version of the GIZMO code is available at <http://www.tapir.caltech.edu/~phopkins/Site/GIZMO.html>.

REFERENCES

Bai X.-N., Stone J. M., 2010, *Astrophys. J. Supp.*, 190, 297

- Blum J., 2018, *Space Sci. Rev.*, 214, 52
 Chiang E., Youdin A. N., 2010, *Ann. Rev. Planet. Earth Sci.*, 38, 493
 Dharmawardena T. E., Kemper F., Scicluna P., Wouterloot J. G. A., Trejo A., Srinivasan S., Cami J., Zijlstra A., Marshall J. P., 2018, *Mon. Not. R. Astron. Soc.*, 479, 536
 Draine B., 2010, *Physics of the Interstellar and Intergalactic Medium*. Princeton Series in Astrophysics, Princeton University Press
 Draine B. T., 2003, *Ann. Rev. Astron. Astrophys.*, 41, 241
 Draine B. T., Fraisse A. A., 2009, *Astrophys. J.*, 696, 1
 Draine B. T., Salpeter E. E., 1979, *Astrophys. J.*, 231, 77
 Falkovich G., Fouxon A., Stepanov M. G., 2002, *Nature*, 419, 151
 Federrath C., 2013, *Mon. Not. R. Astron. Soc.*, 436, 1245
 Garaud P., Meru F., Galvagni M., Olczak C., 2013, *Astrophys. J.*, 764, 146
 Habing H. J., 1996, *Astron. Astrophys. Rev.*, 7, 97
 Haugen N. E. L., Brandenburg A., Sandin C., Mattsson L., 2021, arXiv e-prints, p. arXiv:2105.01539
 Höfner S., Olofsson H., 2018, *Astron. Astro. Rev.*, 26, 1
 Hopkins P. F., 2015, *Mon. Not. R. Astron. Soc.*, 450, 53
 Hopkins P. F., Lee H., 2016, *Mon. Not. R. Astron. Soc.*, 456, 4174
 Hopkins P. F., Rosen A. L., Squire J., Panopoulou G. V., Soliman N. H., Seligman D., Steinwandel U. P., 2021, arXiv e-prints, p. arXiv:2107.04608
 Hopkins P. F., Squire J., 2018a, *Mon. Not. R. Astron. Soc.*, 480, 2813
 Hopkins P. F., Squire J., 2018b, *Mon. Not. R. Astron. Soc.*, 479, 4681
 Hopkins P. F., Squire J., Seligman D., 2020, *Mon. Not. R. Astron. Soc.*, 496, 2123
 Ishibashi W., Fabian A. C., 2015, *Mon. Not. R. Astron. Soc.*, 451, 93
 Kato T., 2013, *Perturbation theory for linear operators*. Grundlehren der mathematischen Wissenschaften, Springer Berlin Heidelberg
 Knapp G. R., 1985, *Astrophys. J.*, 293, 273
 Konstantin L., Schmidt W., Girichidis P., Peters T., Shetty R., Klessen R. S., 2016, *Mon. Not. R. Astron. Soc.*, 460, 4483
 Krapp L., Benítez-Llambay P., Gressel O., Pessah M. E., 2019, *Astrophys. J. Lett.*, 878, L30
 Krapp L., Youdin A. N., Kratter K. M., Benítez-Llambay P., 2020, *Mon. Not. R. Astron. Soc.*, 497, 2715
 Krumholz M. R., Thompson T. A., 2012, *Astrophys. J.*, 760, 155
 Li X.-Y., Mattsson L., 2020, *Astrophys. J.*, 903, 148
 Mathis J. S., Rumpl W., Nordsieck K. H., 1977, *Astrophys. J.*, 217, 425
 Mattsson L., Bhatnagar A., Gent F. A., Villarroel B., 2019, *Mon. Not. R. Astron. Soc.*, 483, 5623
 Maxey M. R., 1987, *Phys. Fluids*, 30, 1915
 McNally C. P., Lovascio F., Paardekooper S.-J., 2021, *Mon. Not. R. Astron. Soc.*, 502, 1469
 Ménard B., Scranton R., Fukugita M., Richards G., 2010, *Mon. Not. R. Astron. Soc.*, 405, 1025
 Micelotta E. R., Matsuura M., Sarangi A., 2018, *Space Sci. Rev.*, 214, 53
 Moro J., Dopico F. M., 2002, in , *Applied Mathematics and Scientific Computing*. Springer US, pp 143–175
 Moseley E. R., Squire J., Hopkins P. F., 2019, *Mon. Not. R. Astron. Soc.*, 489, 325
 Murray N., Quataert E., Thompson T. A., 2005, *Astrophys. J.*, 618, 569

- Norris B. R. M., Tuthill P. G., Ireland M. J., Lacour S., Zijlstra A. A., Lykou F., Evans T. M., Stewart P., Bedding T. R., 2012, *Nature*, 484, 220
- Ormel C. W., Cuzzi J. N., 2007, *Astron. Astro.*, 466, 413
- Paardekooper S.-J., McNally C. P., Lovascio F., 2020, *Mon. Not. R. Astron. Soc.*, 499, 4223
- Paardekooper S.-J., McNally C. P., Lovascio F., 2021, *Mon. Not. R. Astron. Soc.*, 502, 1579
- Pan L., Padoan P., 2013, *Astrophys. J.*, 776, 12
- Pan L., Padoan P., 2014, *Astrophys. J.*, 797, 101
- Pan L., Padoan P., Scalo J., 2014a, *Astrophys. J.*, 791, 48
- Pan L., Padoan P., Scalo J., 2014b, *Astrophys. J.*, 792, 69
- Pumir A., Wilkinson M., 2016, *Ann. Rev. Condensed Matter Phys.*, 7, 141
- Scoville N., 2003, *J. Korean Astron. Soc.*, 36, 167
- Seligman D., Hopkins P. F., Squire J., 2019, *Mon. Not. R. Astron. Soc.*, 485, 3991
- Squire J., Hopkins P. F., 2018a, *Astrophys. J.*, 856, L15
- Squire J., Hopkins P. F., 2018b, *Mon. Not. R. Astron. Soc.*, 477, 5011
- Squire J., Hopkins P. F., 2020, *Mon. Not. R. Astron. Soc.*, 498, 1239
- Squire J., Hopkins P. F., Quataert E., Kempinski P., 2021, *Mon. Not. R. Astron. Soc.*, 502, 2630
- Squires K. D., Eaton J. K., 1990, *Phys. Fluids A*, 2, 1191
- Steinwandel et al., 2021, in preparation
- Sundaram S., Collins L. R., 1997, *J. Fluid Mach.*, 335, 75
- Thompson T. A., Quataert E., Murray N., 2005, *Astrophys. J.*, 630, 167
- Voelk H. J., Jones F. C., Morfill G. E., Roeser S., 1980, *Astron. Astro.*, 85, 316
- Wallström S., Dharmawardena T., Rodríguez Marquina B., Sci-cluna P., Srinivasan S., Kemper F., NESS Collaboration 2019, in Kerschbaum F., Groenewegen M., Olofsson H., eds, *IAU Symposium Vol. 343 of IAU Symposium, Measuring spatially resolved gas-to-dust ratios in AGB stars*. pp 538–539
- Wang L.-P., Wexler A. S., Zhou Y., 2000, *J. Fluid Mach.*, 415, 117
- Weingartner J. C., Draine B. T., 2001a, *Astrophys. J.*, 548, 296
- Weingartner J. C., Draine B. T., 2001b, *Astrophys. J.*, 553, 581
- Weingartner J. C., Draine B. T., 2001c, *Astrophys. J. Supp.*, 134, 263
- Whittet D. C. B., 1992, *Dust in the galactic environment*
- Wilkinson M., Mehlig B., Bezuglyy V., 2006, *Phys. Rev. Lett.*, 97, 048501
- Woitke P., 2006, *Astron. Astro.*, 452, 537
- Youdin A. N., Goodman J., 2005, *Astrophys. J.*, 620, 459
- Youdin A. N., Johansen A., 2007, *Astrophys. J.*, 662, 613
- Zaichik L. I., Simonin O., Alipchenkov V. M., 2006, *Phys. Fluids*, 18, 035110
- Zhu Z., Yang C.-C., 2021, *Mon. Not. R. Astron. Soc.*, 501, 467
- Zubko V., Dwek E., Arendt R. G., 2004, *Astrophys. J. Supp.*, 152, 211

APPENDIX A: LINEAR BEHAVIOUR

In this extended appendix, we analyse key properties of the acoustic resonant drag instability in the presence of a spectrum of grain sizes. We will show that its behaviour depends strongly on the drift regime described in § 2.2 and Tab. 1: in the constant-drift regime (grain-size dependent acceleration) the instability is very similar to the single-grain acoustic RDI (HS18) because all grains share the

same drift velocity; in the non-constant-drift regime (acceleration independent of grain size), the instability is quite different and generally less virulent at small scales.

Although we consider only the acoustic RDI here, it is worth noting that a number of the features we discuss are shared by other RDIs, which can exhibit a diversity of different behaviors. A spectrum of grains has been shown to dramatically affect the linear growth of the $\mu < 1$ streaming instability in protoplanetary disks (Youdin & Goodman 2005), which is also an RDI. Specifically, for smaller grain sizes, (Krapp et al. 2019) found that growth rates were a strong function of the number of species N_d used to discretize the grain distribution, in some cases being unconverged even for $N_d > 2048$. Subsequent works (Paardekooper et al. 2020; Zhu & Yang 2021; McNally et al. 2021) have explored this further, showing that the instability is robust only for large stopping times or $\mu \gtrsim 1$, also depending somewhat on the size distribution of grains. Similar non-convergent behavior is seen for some mode angles of the acoustic RDI discussed below. However, such behavior is not by any means generic to all RDIs. Krapp et al. (2020) showed that the “settling instability” does not suffer from the same convergence issues, despite its similarity to the streaming instability (the only difference being the direction of dust drift; Squire & Hopkins 2018b). Similarly, Squire et al. (2021) computed analytically the growth rates of magnetized gyroresonant RDIs with charged dust grains, which converge rapidly and easily with N_d to fast growth in the continuum limit. This wide variety of behaviors is also exhibited by our calculations below, with some ranges of mode angles and wavenumbers converging very slowly in N_d and some not. More general exploration of these issues is left to future work.

We first describe the basic set up of the calculations in App. A1, then specialise to the simpler constant-drift case in App. A2, before considering the more general non-constant-drift regime in App. A3. While realistic scenarios will often involve a population of grains that stretches across both regimes, we do not consider this possibility here for simplicity. We also do not consider the magnetic RDIs studied in Hopkins & Squire (2018b) due to their complexity and the wide range of parameter regimes.

A1 General considerations

Our theoretical approach will involve computing linear growth rates by starting from a finite number (N_d) of grain-size species. We then take the limit as $N_d \rightarrow \infty$ with the total mass of grains fixed to obtain results valid in the continuous limit. This is by no means the most efficient approach in all cases (see Paardekooper et al. 2021), but is physically enlightening for understanding the physical causes of different behaviors. We thus define the properties of discrete grain species j : the dust-to-gas-mass ratio μ_j (with $\mu_0 = \sum_j \mu_j$), the relative drift velocity $w_{s,j} = |\mathbf{w}_{s,j}|/c_s$, and the stopping time $t_{s,j}$, which become functions of grain size ϵ_{grain} in the continuous limit. We assume that the quasi-equilibrium involves pressureless dust (i.e., no dust velocity dispersion for all grain sizes),

$$\int_{\epsilon_{\text{grain}}}^{\epsilon_{\text{grain}} + d\epsilon_{\text{grain}}} d\epsilon_{\text{grain}} dv [\mathbf{v} - \mathbf{v}_d(\epsilon_{\text{grain}})][\mathbf{v} - \mathbf{v}_d(\epsilon_{\text{grain}})] f_d(\epsilon_{\text{grain}}; \mathbf{x}, \mathbf{v}) = 0, \quad (\text{A1})$$

which implies that the the dust evolution equation (3) is equivalent to fluid equations for its first two moments:

$$\frac{\partial \rho_d}{\partial t} + \nabla \cdot (\rho_d \mathbf{v}_d) = 0, \quad (\text{A2})$$

$$\frac{\partial \mathbf{v}_d}{\partial t} + \mathbf{v}_d \cdot \nabla (\mathbf{v}_d) = -\frac{\mathbf{v}_d - \mathbf{u}_g}{t_s(\epsilon_{\text{grain}}, \mathbf{v}_d)}. \quad (\text{A3})$$

Here ρ_d and \mathbf{v}_d are each functions of ϵ_{grain} , so N_d copies of Eqs. (A2) and (A3) are needed, each with different stopping times $t_{s,j} = t_s(a_{d,j})$ and $w_{s,j}$. We then linearise Eqs. (1), (2), (A2) and (A3) about the quasi-equilibrium in which the dust and gas accelerate linearly together at the same rate, but allowing for species-dependent velocity offset (see HS18 for more information). Denoting the quasi-equilibrium quantities with $\langle \cdot \rangle$, and moving to the frame in which the gas is stationary this leads to a set of $3(N_d + 1)$ linear equations for the gas density perturbation $\delta\rho_g = (\rho_g - \langle \rho_g \rangle) / \langle \rho_g \rangle$, gas velocity perturbation $\delta\mathbf{u}_g = \mathbf{u}_g$, dust density perturbation $\delta\rho_{d,j} = (\rho_{d,j} - \langle \rho_{d,j} \rangle) / \langle \rho_{d,j} \rangle$, and dust velocity perturbation $\delta\mathbf{v}_{d,j} = \mathbf{v}_{d,j} - \langle \mathbf{v}_{d,j} \rangle = \mathbf{v}_{d,j} - w_{s,j} c_s \hat{z}$:

$$\begin{aligned} \frac{\partial}{\partial t} \begin{pmatrix} \delta\mathbf{D}_1 \\ \vdots \\ \delta\mathbf{D}_j \\ \vdots \\ \delta\mathbf{F} \end{pmatrix} &= \mathbb{T} \cdot \begin{pmatrix} \delta\mathbf{D}_1 \\ \vdots \\ \delta\mathbf{D}_j \\ \vdots \\ \delta\mathbf{F} \end{pmatrix} = \begin{pmatrix} \mathcal{A}_1 & 0 & 0 & 0 & C_1 \\ 0 & \ddots & 0 & 0 & \vdots \\ 0 & 0 & \mathcal{A}_j & 0 & C_j \\ 0 & 0 & 0 & \ddots & \vdots \\ \mathcal{T}_1 & \dots & \mathcal{T}_j & \dots & \mathcal{F} \end{pmatrix} \cdot \begin{pmatrix} \delta\mathbf{D}_1 \\ \vdots \\ \delta\mathbf{D}_j \\ \vdots \\ \delta\mathbf{F} \end{pmatrix}, \\ \delta\mathbf{D}_j &= \begin{pmatrix} \delta\rho_{d,j} \\ \delta v_{x,j} \\ \delta v_{z,j} \end{pmatrix}, \quad \delta\mathbf{F} = \begin{pmatrix} \delta\rho_g \\ \delta u_x \\ \delta u_z \end{pmatrix}, \\ \mathcal{A}_j &= \begin{pmatrix} -ik_z w_{s,j} & -ik_x & -ik_z \\ 0 & -ik_z w_{s,j} - \frac{1}{t_{s,j}} & 0 \\ 0 & 0 & -ik_z w_{s,j} - \frac{\tilde{\zeta}_{w,j}}{t_{s,j}} \end{pmatrix}, \\ C_j &= \begin{pmatrix} 0 & 0 & 0 \\ 0 & \frac{1}{t_{s,j}} & 0 \\ -\frac{\zeta_{s,j} w_{s,j}}{t_{s,j}} & 0 & \frac{\tilde{\zeta}_{w,j}}{t_{s,j}} \end{pmatrix}, \quad \mathcal{T}_j = \mu_j \begin{pmatrix} 0 & 0 & 0 \\ 0 & \frac{1}{t_{s,j}} & 0 \\ \frac{w_{s,j}}{t_{s,j}} & 0 & \frac{\tilde{\zeta}_{w,j}}{t_{s,j}} \end{pmatrix}, \\ \mathcal{F} &= \begin{pmatrix} 0 & -ik_x & -ik_z \\ -ic_s^2 k_x & -\sum_i \frac{\mu_i}{t_{s,i}} & 0 \\ -ic_s^2 k_z + \sum_i \frac{\mu_i (\zeta_{s,i} - 1) w_{s,i}}{t_{s,i}} & 0 & -\sum_i \frac{\mu_i \tilde{\zeta}_{w,i}}{t_{s,i}} \end{pmatrix} \quad (\text{A4}) \end{aligned}$$

Here we have considered, without loss of generality, $\mathbf{w}_{s,j} \propto \hat{z}$ and two-dimensional spatial perturbations with wavenumber $\mathbf{k} = (k_x, 0, k_z)$, implying the spatial form of any perturbation is $\propto \exp(ik_x x + ik_z z)$. For convenience below, we will use k and θ_k as variables, with $k_x = k \sin \theta_k$ and $k_z = k \cos \theta_k$. The parameters $\zeta_{s,j}$ and $\tilde{\zeta}_{w,j}$ are the density and velocity dependencies of the stopping time, respectively, which are defined from

$$\frac{\delta t_{s,j}}{\langle t_{s,j} \rangle} = -\zeta_{s,j} \frac{\delta\rho_g}{\langle \rho_g \rangle} - \zeta_{w,j} \frac{\mathbf{w}_{s,j} \cdot (\delta\mathbf{v} - \delta\mathbf{u}_g)}{c_s^2 w_{s,j}^2}, \quad (\text{A5})$$

and $\tilde{\zeta}_{w,j} \equiv \zeta_{w,j} + 1$. For Epstein drag,

$$\zeta_{s,j} = \frac{\gamma + 1 + 2a_\gamma w_{s,j}^2}{2 + 2a_\gamma w_{s,j}^2}, \quad \zeta_{w,j} = \frac{a_\gamma w_{s,j}^2}{1 + a_\gamma w_{s,j}^2}, \quad (\text{A6})$$

with $a_\gamma = 9\pi\gamma/128$. The structure of the matrix (A4), which is nonzero only in the blocks shown, encapsulates the physics of the multi-species dust and gas system; a given species of dust is governed by its own dynamics (block \mathcal{A}_j), the influence of the gas on species j (block C_j), the influence of species j on the gas (block $\mu_j \mathcal{T}_j$), and the dynamics of the gas itself (block \mathcal{F}). Importantly,

there is no direct coupling between grain species, which would manifest in the matrix structure as off-diagonal blocks other than C_j and \mathcal{T}_j . The system exhibits linear instability if eigenvalue(s) of the matrix $i\mathbb{T}$ have a positive imaginary part.

To simplify some integrals in the sections below, we will assume grains with an MRN mass distribution ($d\mu/d \ln \epsilon_{\text{grain}} \propto \epsilon_{\text{grain}}^{1/2}$ between $\epsilon_{\text{grain}}^{\min}$ and $\epsilon_{\text{grain}}^{\max}$), which implies

$$\frac{d\mu}{d\epsilon_{\text{grain}}} = \frac{\mu_0}{2} \frac{\epsilon_{\text{grain}}^{-1/2}}{(\epsilon_{\text{grain}}^{\max})^{1/2} - (\epsilon_{\text{grain}}^{\min})^{1/2}}, \quad (\text{A7})$$

where μ_0 is the total dust-to-gas mass ratio. We also assume dust is drifting in the supersonic regime with Epstein drag, which implies $t_s \propto \epsilon_{\text{grain}}$ and $w_s \sim \text{const.}$ for the constant-drift regime, and $t_s \propto \epsilon_{\text{grain}}^{1/2}$, $w_s \propto \epsilon_{\text{grain}}^{1/2}$ for the non-constant-drift regime.

A2 Constant-drift regime

In this section we specialise to the case where the acceleration imparted on grains by the radiative forcing scales as $a^{\text{ext}} \propto 1/\epsilon_{\text{grain}}$, as relevant when $\epsilon_{\text{grain}} \lesssim \lambda_{\text{rad}}$ (see §2.2; Weingartner & Draine 2001c). Importantly, in this regime, all grains share the same drift velocity $w_{s,j}$, which significantly simplifies the linear mode structure compared to the more general case. The growth rate of the fastest-growing modes at moderate k can be straightforwardly obtained using arguments similar to those of Squire & Hopkins (2018a), which are based on perturbing the eigenvalues of the matrix in the small parameter μ . To generalize to the case with a spectrum of grains, we assume that all μ_j are of the same order such that $\mu_j = \mu \bar{\mu}_j$ with $\bar{\mu}_j \sim O(1)$, then treat the parts of \mathbb{T} that contain μ (\mathcal{T}_j and part of \mathcal{F}) as a perturbation; i.e., $\mathbb{T} = \mathbb{T}_0 + \mu \mathbb{T}^{(1)}$. One then notes that at the specific ‘‘resonant’’ mode angle, when $w_{s,j} \cos \theta_k = 1$, the unperturbed system ($\mathbb{T}|_{\mu=0}$) is $N_d + 1$ degenerate and 2-fold defective (there are only N_d eigenvectors). Physically, this is where the sound-wave frequency $\omega_F = k c_s$ matches the streaming frequency ($\omega_{D,j} = k_z c_s w_{s,j}$) of all dust species. By standard linear algebra arguments (Kato 2013; Moro & Dopico 2002), in order to compute the eigenvalues of the perturbed system, one should perform a similarity transformation of \mathbb{T}_0 and $\mathbb{T}^{(1)}$ to form a block that is as close to diagonal as possible with $\omega_0 = \omega_F = \omega_{D,j}$ along the diagonal. This yields a transformed \mathbb{T}_0 of the form

$$\tilde{\mathbb{T}}_0 = \begin{pmatrix} \omega_0 & 0 & 0 & 0 & c_1 \\ 0 & \ddots & 0 & 0 & \vdots \\ 0 & 0 & \omega_0 & 0 & c_j \\ 0 & 0 & 0 & \ddots & \vdots \\ 0 & \dots & 0 & \dots & \omega_0 \end{pmatrix}, \quad (\text{A8})$$

while $\mathbb{T}^{(1)}$ transforms to

$$\tilde{\mathbb{T}}^{(1)} = \begin{pmatrix} \cdot & \cdot & \cdot & \cdot & \cdot \\ \cdot & \cdot & \cdot & \cdot & \cdot \\ \cdot & \cdot & \cdot & \cdot & \cdot \\ \cdot & \cdot & \cdot & \cdot & \cdot \\ t_{F,1} & \dots & t_{F,j} & \dots & t_{F,F} \end{pmatrix} \quad (\text{A9})$$

(where it transpires that most of $\tilde{\mathbb{T}}^{(1)}$ will not be needed). Here $c_j = \xi_{D,j}^L \cdot C_j \cdot \xi_F^R$ and $t_{F,j} = \xi_F^L \cdot \mathcal{T}_j \cdot \xi_{D,j}^R$ are now scalars, with ξ_F^R (ξ_F^L) the right (left) eigenvector of $\mathcal{F}|_{\mu=0}$ and $\xi_{D,j}^R$ ($\xi_{D,j}^L$) the right (left) eigenvector of \mathcal{A}_j . One then computes the eigenvalues of $\tilde{\mathbb{T}}_0 + \mu \tilde{\mathbb{T}}^{(1)}$ by noting that for $\mu \ll 1$, the dominant balance solution for $\omega^{(1)} =$

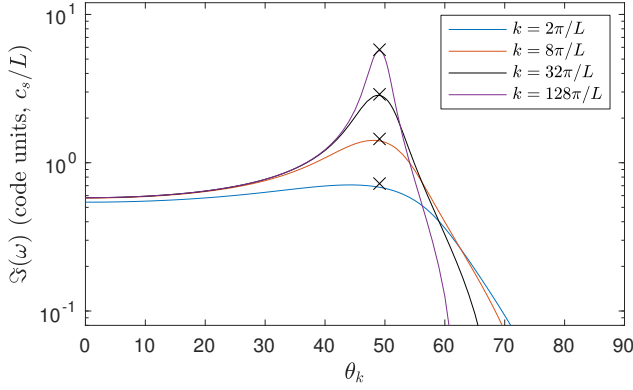


Figure A1. Linear growth rate as a function of mode angle θ_k for the parameters of the constant-drift simulation from the main text. Different coloured curves show wavenumbers relevant to the largest scales of the box (blue curve), down to several resolution elements (purple curves). Black crosses show the analytic prediction (A11), illustrating the accurate prediction of the fastest growing mode angle and growth rate. The numerical growth-rate calculation is discretised with $N_d = 128$ species of grains, but results are almost independent of N_d .

$\omega - \omega_0$ scales as $\sim \mu^{1/2}$ and is

$$\omega^{(1)} = \pm \mu^{1/2} \left(\sum_j t_{F,j} c_j \right)^{1/2} + \mathcal{O}(\mu). \quad (\text{A10})$$

Thus, while the full $\mathcal{O}(\mu)$ solution for $\omega^{(1)}$ is very complex and depends on all components of $\mathbb{T}^{(1)}$ ($t_{F,F}$ and other components in Eq. (A9)), the growth rate at resonance ($w_{s,j} \cos \theta_k = 1$) is straightforward to derive and larger than the growth rate at any other θ_k (because $\mu^{1/2} \gg \mu$ for $\mu \ll 1$). Inserting the matrices from Eq. (A4) to compute $t_{F,j}$ and c_j , we find a remarkably simple expression for the growth rate at the resonant mode angle $\cos \theta_k = 1/w_{s,j}$,

$$\begin{aligned} \Im(\omega) &\approx \frac{1}{2} \left[k c_s \sum_j \mu_j \frac{1}{t_{s,j}} \left(1 - \frac{\zeta_{s,j}}{\tilde{\zeta}_{w,j}} \right) \right]^{1/2} \\ &\approx \frac{1}{2} \left[k c_s \int d\epsilon_{\text{grain}} \frac{d\mu}{d\epsilon_{\text{grain}}} \frac{1}{t_s(\epsilon_{\text{grain}})} \left(1 - \frac{\zeta_s}{\tilde{\zeta}_w} \right) \right]^{1/2} \\ &\approx \frac{\mu_0^{1/2}}{2} \left[\frac{k c_s}{t_{s,\text{max}}} \sqrt{\frac{\epsilon_{\text{grain}}^{\text{max}}}{\epsilon_{\text{grain}}^{\text{min}}}} \left(1 - \frac{\zeta_s}{\tilde{\zeta}_w} \right) \right]^{1/2}, \end{aligned} \quad (\text{A11})$$

where we convert to a continuous distribution on the second line, and specialise to an MRN distribution of supersonically drifting grains on the third line (with $t_{s,\text{max}}$ the stopping time of the maximum grain size). Note that, like w_s , ζ_s and $\tilde{\zeta}_w$ are independent of ϵ_{grain} in the constant-drift regime.

As in the single-grain case (see HS18), Eq. (A11) is valid for $\mu \ll k c_s t_s(\epsilon_{\text{grain}}) \ll \mu^{-1}$. At very short wavelengths ($k c_s t_s \gg \mu^{-1}$) the growth rate keeps a similar structure but transitions to scaling as $\sim \mu^{1/3} k^{1/3}$; we do not consider this in detail because it is a difficult regime to study numerically (see HS18 and MSH19). At very long wavelengths ($k c_s t_s \ll \mu$) the growth rate loses its resonant character and scales with $\sim \mu^{1/3} k^{2/3}$; this case is considered below (App. A3.1) because it the growth rate does not depend strongly on all grains having the same w_s (see Eq. (A15)).

We plot linear growth rates for the same parameters as the nonlinear constant-drift RDI simulation in the main text as a function of θ_k in Fig. A1. The different lines show a number of different

k relevant to the simulation size. The analytic result, Eq. (A11), is shown with the black crosses, and clearly provides a very accurate approximation to the maximum growth rate and wave number. The general features of the instability are very similar to the single-grain case, with a resonant peak that scales as $\Im(\omega) \sim \mu_0^{1/2}$ and increases in sharpness towards small scales.

A3 Non-constant-drift regime

In the non-constant-drift regime, which is appropriate when $\epsilon_{\text{grain}} \gtrsim \lambda_{\text{rad}}$, or when a force accelerates the gas rather than the dust, the population of grains no longer share the same drift velocity. This significantly complicates the analysis of the resonant modes compared to that of App. A2, and useful analytic expressions for the growth rates are much harder to obtain. Further, in some regimes the growth rate scales with the number of dust species N_d , and care is required even for the interpretation of numerically computed growth rates (this also occurs in many regimes for the streaming instability in protoplanetary disks, see Krapp et al. 2019; Paardekooper et al. 2021). For this reason, we provide only a cursory survey of different modes and regimes here, pointing out some key features of how the growth rate varies with wavelength, but forgoing a full detailed analysis. As in HS18 we will organise the results by the type of mode, describing the most important modes across different regimes. Further details of the mode structure, growth rates, and possible instabilities that can occur with different drag laws are given in HS18.

A3.1 Low- k modes

At very long wavelengths, $k c_s t_s \ll \mu$, the system exhibits a non-resonant instability that is insensitive to the distribution of grain velocities and sizes. One can derive its growth rate using the same analysis as HS18, starting from the dispersion relation (characteristic polynomial of \mathbb{T}). Making the substitution $\kappa_{\parallel} = k c_s \cos \theta_k$ and assuming $w_{s,i} \sim \mathcal{O}(1)$, one assumes $\omega \sim \kappa_{\parallel}^{2/3}$ and expands the dispersion relation in $\kappa_{\parallel} \ll 1$. This process, which is straightforwardly carried out for $N_d = 1, 2, 3$, or 4 using a computer algebra system, shows that the growth rate for arbitrary N_d is the obvious generalisation of the single-species case,

$$\Im(\omega) \approx \frac{1}{2} \left[\frac{1}{1 + \sum_j \mu_j} \sum_j \mu_j \frac{w_{s,j}^2}{t_{s,j}} \left(1 - \frac{\zeta_{s,j}}{\tilde{\zeta}_{w,j}} \right) (k c_s \cos \theta_k)^2 \right]^{1/3} \quad (\text{A12})$$

(taking $\tilde{\zeta}_{w,j} > \zeta_{s,j}$ as relevant to Epstein drag). Replacing the sum with an integral and assuming $\mu \ll 1$ then yields the growth rate for a continuous spectrum of grains, rate

$$\Im(\omega) \approx \frac{1}{2} \left[\int d\epsilon_{\text{grain}} \frac{d\mu}{d\epsilon_{\text{grain}}} \frac{w_s^2(\epsilon_{\text{grain}})}{t_s(\epsilon_{\text{grain}})} \left(1 - \frac{\zeta_s(\epsilon_{\text{grain}})}{\tilde{\zeta}_w(\epsilon_{\text{grain}})} \right) (k c_s \cos \theta_k)^2 \right]^{1/3}. \quad (\text{A13})$$

Considering first the non-constant-drift regime, Eq. (A13) can be simplified to

$$\Im(\omega) \approx \frac{\mu_0^{1/3}}{2} \left[\frac{w_{s,\text{max}}^2 - w_{s,\text{min}}^2}{t_{s,\text{max}} - t_{s,\text{min}}} \left(1 - \frac{\zeta_s}{\tilde{\zeta}_w} \right) (k c_s \cos \theta_k)^2 \right]^{1/3}, \quad (\text{A14})$$

by assuming constant- a^{ext} supersonic drift with an MRN distribution. (To obtain a simple result for the integral, we neglect the grain-size dependence of ζ_s and $\tilde{\zeta}_w$; the dependence is minor for supersonic drift, with $\zeta_s/\tilde{\zeta}_w = 1/2 + \mathcal{O}(w_s^{-2})$.)

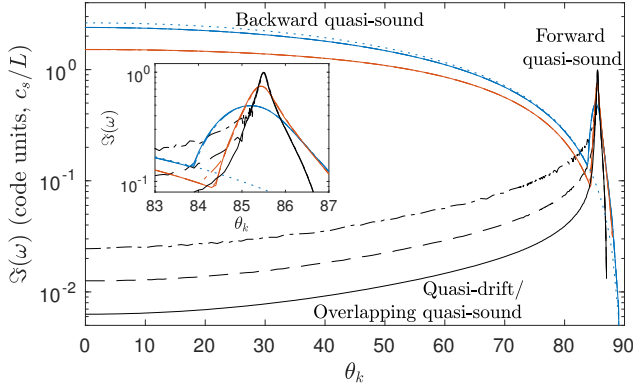


Figure A2. Linear growth rate as a function of mode angle θ_k for the parameters of the non-constant-drift RDI simulation from the main text. As in Fig. A1, different coloured curves show different representative wavenumbers; $k = 2\pi/L$ (blue curves), $k = 8\pi/L$ (red curves), $k = 32\pi/L$ (black curves). Different line styles show different grain-discretisation resolutions – $N_d = 256$ (dot dashed), $N_d = 512$ (dashed), and $N_d = 1024$ (solid) – to illustrate the convergence (or lack thereof) to the continuous limit. When the backwards quasi-sound mode is unstable at $k c_s t_s \lesssim w_s^{-1}$ (Eq. (A17)), this dominates the growth rate for nearly parallel modes and is well converged in N_d , with a growth rate that is accurately predicted by the analytic expression (A18), shown with the blue dotted line for $k = 2\pi/L$. At higher k , we see the non-convergence of the quasi-drift modes (black curves at near-parallel angles) as discussed in A3.2.1 and/or the overlapping resonant quasi-sound modes discussed in A3.2.2. Finally, at $\theta_k \approx 85.5$ – the mode angle resonant with the fastest grains – we see a converged resonant, forward quasi-sound mode (see inset, which zooms in on this region), with a growth rate that increases with k . This mode is responsible for the formation of the filamentary structure of large dust grains seen in Fig. 3.

Because the growth mechanism is non-resonant, the same argument also applies in the constant-drift regime when $k c_s t_s \ll \mu$, in which case Eq. (A13) simplifies to

$$\Im(\omega) \approx \frac{\mu_0^{1/3}}{2} \left[\frac{w_s^2}{t_{s,\max}} \sqrt{\frac{\epsilon_{\text{grain}}^{\max}}{\epsilon_{\text{grain}}^{\min}}} \left(1 - \frac{\zeta_s}{\zeta_w} \right) (k c_s \cos \theta_k)^2 \right]^{1/3}. \quad (\text{A15})$$

Equations (A14) and (A15) match numerical solutions of the dispersion relation perfectly (not shown).

A3.2 Quasi-drift and quasi-sound modes

In the shorter wavelength regime, HS18 identifies two types of (possibly) unstable modes: “quasi-drift” modes, so named because they are a perturbed drifting dust-density mode with real frequency $\Re(\omega) \approx k_z c_s w_{s,j}$, and “quasi-sound” modes, which are perturbed sound waves with real frequency $\Re(\omega) = \pm k c_s$. The two modes behave very differently in the presence of a spectrum of grain velocities, with the quasi-drift modes disappearing in the continuous limit as the density of each grain species tends to zero. The growth rates of each can be derived by perturbing the eigenvalues of the $\mu = 0$ operator, $\mathbb{T}_0 = \mathbb{T}|_{\mu=0}$ (see Eq. (A4)), in the small parameter $\mu \sim \mu_i$ with $\mu \mathbb{T}^{(1)} = \mathbb{T} - \mathbb{T}_0$. Standard matrix perturbation theory is valid, implying that $\omega = \omega_0 + \mu \omega^{(1)}$ with $\omega^{(1)} = \xi_0^L \cdot \mathbb{T}^{(1)} \cdot \xi_0^R$, where ξ_0^R (ξ_0^L) is the right (left) eigenmode of \mathbb{T}_0 for the (drift or sound) mode that is being perturbed (with $\xi_0^L \cdot \xi_0^R = 1$). In the single-grain-species (or constant drift) instability, the two modes coalesce at the resonant angle, $w_s \cos \theta_k = 1$, where the standard perturbation theory results become invalid because of the defective structure of the

matrix (see App. A2; Squire & Hopkins 2018a). Below, we discuss the quasi-drift then quasi-sound modes in turn, arguing that the quasi-drift mode disappears in the limit of a continuous grain velocity distribution, while both forward and backward propagating quasi-sound modes remain relevant.

A3.2.1 Quasi-drift modes The quasi-drift mode is derived by choosing ξ_0^R and ξ_0^L as the drift mode for species j , with frequency $\omega_0 = k_z c_s w_{s,j}$. Because of the structure of $\mathbb{T}^{(1)}$ and the eigenmodes ξ_0^R and ξ_0^L , it transpires that the frequency perturbation $\omega^{(1)}$ scales with μ_j , *viz.*, the dust-to-gas mass ratio of the *individual* grain species.¹¹ Importantly, this implies that the growth rate approaches zero as $N_d \rightarrow \infty$; instead of a smaller number of fast-growing modes, there is a continuum of modes with an infinitesimally small growth rate. This behaviour is seen for the nearly parallel (small θ_k) modes at small scales (black curves) in Fig. A2: the growth rate scales approximately as $\sim N_d^{-1}$, thus disappearing in the continuous limit.

A3.2.2 Quasi-sound modes The quasi-sound mode is derived by choosing ξ_0^R and ξ_0^L as the eigenmode for a sound wave at $\mu = 0$, with frequency $\omega_0 = k c_s$. Unlike the quasi-drift modes, the structure of ξ_0^R and ξ_0^L in this case imply that the perturbed frequency is the *sum* of the perturbed frequencies from each individual grain species. In other words, if we define $\omega_j^{(1)}$ as the frequency perturbation to arise if only μ_j is nonzero, with all other $\mu_i = 0$, then $\omega^{(1)} = \sum_j \omega_j^{(1)}$. This implies that the growth rate (away from resonant regions) scales with $\mu_0 = \sum_j \mu_j$ and so can be rapid in the continuum limit. Using this knowledge, it is straightforward to derive the continuum growth/damping rate of the backwards propagating mode. While the full expression is complex and unenlightening, it is straightforward to show that the mode is unstable ($\Im(\omega) > 0$) for

$$k c_s t_{s,j} < \frac{w_{s,j}^2}{(1 + w_{s,j})^2 [\zeta_{w,j} + w_{s,j}(\zeta_{s,j} - 1)]} \zeta_{w,j}^2 \left(1 - \frac{\zeta_{s,j}}{\zeta_{w,j}} \right) \approx \frac{1}{w_{s,j}} + \mathcal{L}(w_{s,j}^{-2}) \quad (\text{Epstein Drag}), \quad (\text{A17})$$

and a simple expression for the unstable regime is found through an expansion in small $k c_s t_s$:

$$\begin{aligned} \Im(\omega) &\approx \frac{1}{2} \sum_j \mu_j \frac{w_{s,j}^2 \cos^2 \theta_k}{t_{s,j} (1 + w_{s,j} \cos \theta_k)} \left(1 - \frac{\zeta_{s,j}}{\zeta_{w,j}} \right) + \mathcal{O}(k c_s t_s), \\ &\approx \frac{1}{2} \int d\epsilon_{\text{grain}} \frac{d\mu}{d\epsilon_{\text{grain}}} \frac{w_s^2 \cos^2 \theta_k}{t_s (1 + w_s \cos \theta_k)} \left(1 - \frac{\zeta_s}{\zeta_w} \right). \end{aligned} \quad (\text{A18})$$

We see that the backwards mode can provide a positive growth rate at wavelengths shorter (up to $k c_s t_{s,j} \approx w_{s,j}^{-1}$) than the low- k regime of App. A3.1.¹² The expression (A18) is plotted with the blue-dotted line on top of the numerically computed growth rate for the parameters of the non-constant-drift simulation in Fig. A2, showing good agreement. By comparison to the nonlinear evolution shown in Figs. 3 and 4, we see that this mode is a significant

¹¹ Specifically, the growth rate for the drift mode of species j is

$$\Im(\omega) = \mu_j \frac{1}{t_{s,j}} \frac{w_{s,j}^2 \cos^2 \theta_k}{w_{s,j}^2 \cos^2 \theta_k - 1} \left(1 - \frac{\zeta_{s,j}}{\zeta_{w,j}} \right), \quad (\text{A16})$$

which is the same as the single-species result (equation (13) of HS18).

¹² The expression (10) in HS18 is the higher- k expression for the same mode.

driver of the box-scale instability and causes the formation of the shock wave in this simulation (see Fig. 3).

The behaviour of the forward-propagating quasi-sound mode is significantly more complex because of the presence of resonances, which overlap with each other due to the distribution of $w_{s,j}$. This leads to a complicated dependence of the growth rate on the width of the resonance (which gets narrower with increasing $k c_s t_s$) and the distribution of grains. This makes it difficult and subtle to predict analytically, and even to solve for numerically in the short-wavelength regime, features that are shared by the streaming instability in protoplanetary disks. Its basic attributes are best explained through considering the contribution of an individual grain species ($\omega_j^{(1)}$), along with reference to numerically computed growth rate in Fig. A2. Like for the backward quasi-sound mode discussed above, direct calculation of $\omega_j^{(1)}$ yields a complex expression that we do not reproduce in full here. Its key feature is that $\Im[\omega_j^{(1)}(\theta_k)]$ is everywhere negative except close the resonant angle $w_{s,j} \cos \theta_{k,j} = 1$, where it has the form

$$\Im(\omega_j^{(1)}) \propto \frac{1}{1 - w_{s,j} \cos \theta_k} + \dots \quad (\text{A19})$$

Although the infinity at resonance is spurious (it is regularised by the expansion in μ_j becoming invalid), the general form of Eq. (A19) shows that quasi-sound modes are very unstable for $\theta_k > \theta_{k,j}$ and highly damped for $\theta_k < \theta_{k,j}$. The width of this region of sudden change in $\Im(\omega)$ (i.e., the width of the resonance) decreases with increasing $k c_s t_s$. In the presence of a wide spectrum of grains, where the total growth rate is $\sum_j \omega_j^{(1)}$, these positive and negative growth rates cancel out between different grains in the regions of θ_k where resonances overlap. This behaviour is seen for $\theta_k \lesssim 80^\circ$ in Fig. A2, where, despite the presence of resonant grains the growth rate is unconverged in N_d (recall that the non-constant-drift simulation in the main text has grains from $w_{s,j} \approx 1$ to 12; see § 2.4).¹³ Further discussion of similar issues can be found in Krapp et al. (2019, 2020); Paardekooper et al. (2021). However, towards the end of the range of resonant angles, as $\cos \theta_k$ approaches $w_{s,\max}^{-1}$, there no longer exist resonances at higher θ_k , which suggests the existence of a converged, resonant growth region around the resonance of the largest grains $\cos \theta_{k,w_{s,\max}} = 1$. Indeed, this is seen in the inset of Fig. A2, where we see fast growth rates around $\theta_k \approx 85.5^\circ \approx \cos^{-1}(w_{s,\max}^{-1})$, which are converged to the continuum limit (overlapping dot-dashed, dashed, and solid lines). Further, we see that the growth rate increases with k , albeit more slowly than the single-grain case (which scales as $\Im(\omega) \sim k^{1/2}$) because at higher k , the resonant width narrows, so there is a smaller population of grains that contribute to the converged peak. Thus, we see that a resonant mode survives in the presence of a continuous spectrum of grains, although only the largest grains (which stream the fastest) can contribute to its growth rate, which is therefore reduced compared to the constant-drift (or single grain) regime (Fig. A1).

APPENDIX B: LINEAR GROWTH IN GIZMO

As discussed above, a number of recent works have explored the difficulty of numerically resolving the linear growth of polydisperse dust instabilities in the context of protoplanetary disks (the streaming instability; Krapp et al. 2019; Paardekooper et al. 2021;

¹³ Note that there are also contributions from the quasi-drift modes at these angles, the growth rate of which also decreases with N_d in a similar way.

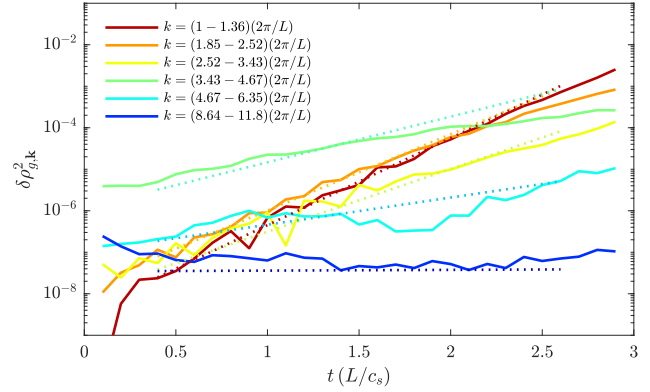


Figure B1. Time evolution of parallel ($\theta_k = 0$, $\hat{\mathbf{k}} = \hat{\mathbf{w}}_s$) modes in the L1Nd1 simulation (see text). The solid lines show the Fourier energy of gas density perturbations at the labeled k from the box scales (red) to small scales (blue). The dashed lines show $\exp(2\gamma_{\text{lin}} t)$ (arbitrarily rescaled in amplitude), where γ_{lin} is computed from the dispersion relation as described in App. A for the same k and $N_d = 256$.

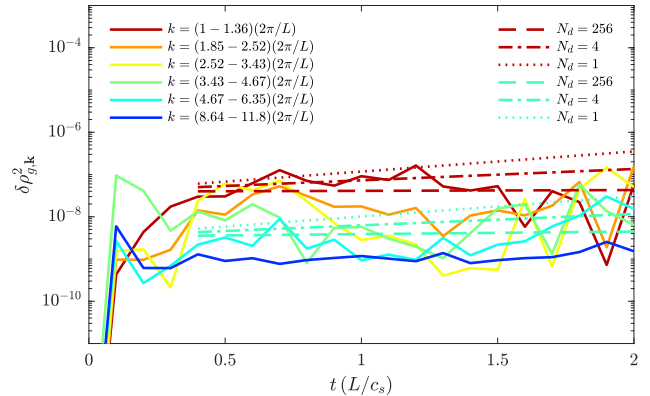


Figure B2. As for Fig. B1, but for the LsmallNd1, which is identical to L1Nd1 but 12 times smaller. The higher k of the box scale suppresses the backward quasi-sound mode (see Fig. A2), making the growth rate of all parallel modes effectively zero in the $N_d \rightarrow \infty$ limit. The dashed, dot-dashed, and dotted lines show the linear growth rate of the box-scale modes when computed with different numbers of grain-size bins, as labelled. The simulation appears inconsistent with $N_d \lesssim 4$, for which there should be a positive growth rate, suggesting that the continuous grain limit is at least approximately resolved by GIZMO.

Zhu & Yang 2021). The fundamental problem relates to the discretization of the dust size into N_d bins, as there can be very slow (or nonexistent) convergence to the continuous limit as $N_d \rightarrow \infty$. Indeed, the origin of this issue is clear for some of modes discussed in App. A3; for example, the growth rate of “quasi-drift modes” (App. A3.2) scales linearly with the relative density of an individual grain size, which approaches zero as $N_d \rightarrow \infty$ (see Fig. A2). As also discussed above (see Fig. A1), this issue is relevant only for the non-constant-drift regime, and in the constant-drift regime, linear results are well converged even at relatively small N_d .

In this appendix, we assess the relevance of such effects to our nonlinear simulations, by computing linear growth rates in their early phases. We focus on only the non-constant-drift case and the particular concern of resolving spuriously large growth rates due to insufficient resolution in dust size space. The method also acts

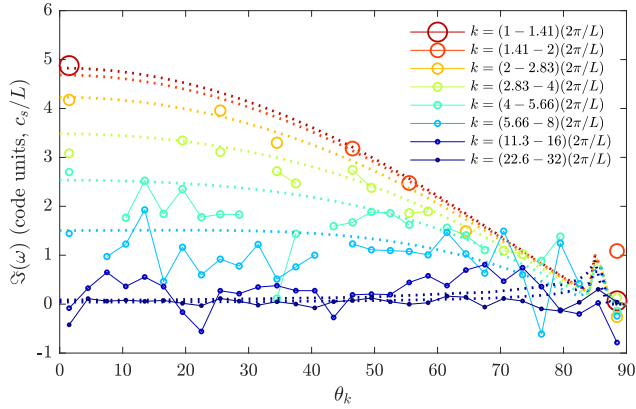


Figure B3. Points and solid lines show the growth rates as a function of $k = |\mathbf{k}|$ and θ_k measured from the high-resolution non-constant-drift simulation discussed in the main text. We measure each growth rate by fitting each Fourier mode of the gas density to an exponential in time for $t \leq 3$. At larger scales, there are many fewer Fourier mode angles available because of the discretization of \mathbf{k} in the box, which explains the sparse points for larger scale modes (red colors). The dashed lines show the linearly computed growth rate as a function of θ_k (as also shown in Fig. A2) for each of the bins in k .

as a stringent test of the ability of GIZMO to resolve the linear physics of the RDI more generally. Note, however, that because this method uses the nonlinear results to probe the linear physics, modes can in principle interact; for example, a mode that is linearly neutral or damped may grow due to the nonlinear interactions even at small amplitudes. In addition, meshless methods such as that used by GIZMO are inherently relatively noisy for low amplitude fluctuations, which implies that the linear growth phase starts from relatively larger amplitudes (compared to a fixed-mesh numerical method) and makes resolving the linear phase more difficult.

Our method involves using a Fourier decomposition of the gas density in the simulation to compute the time evolution of individual Fourier modes. We then bin these in $k = |\mathbf{k}|$ and $\theta_k = \cos^{-1}(k_z/k)$ to compare to the predicted rates at a given scale and mode angle. As can be seen from Fig. A2, the non-convergent linear behavior manifests itself only at rather small scales, approximately 10 times smaller than the box scale and smaller. Thus, in order to correctly assess the effect and ensure that it is not unduly influenced by numerical dissipation between gas elements, we have run two extra simulations. The first, which we label L1Nd1, is identical to the non-constant-drift case in the main text, with box size $L_0 = 1$ in code units, but with 128^3 gas resolution elements and the same number of dust elements. The second, labeled LsmallNd1, has a box size L_{small} that is 12 times smaller, $L_{\text{small}} = L_0/12$, so as to more directly resolve the small-scale dynamics (this also makes it significantly more computationally expensive). We stress that because these simulations use the same number of dust and gas elements, they should be a more stringent test of the features we wish to study (non-convergence in N_d) compared to the simulations of the main text, which used 4×256^3 dust elements and 256^3 gas elements (the purpose of the L1Nd1 simulation is to more appropriately compare to the LsmallNd1 simulation). As for the simulations in the main text, the dust is discretized in size by sampling from a continuous distribution.

The results of these two simulations are shown in Figs. B1 and B2. We illustrate just the parallel modes here – i.e., $\theta_k = 0$ or $\hat{\mathbf{k}} = \hat{\mathbf{w}}_s$ – which are the “backwards quasi-sound” and/or “quasi-

drift” modes at these parameters. Comparing the numerical (solid) and linear (dotted) results in Fig. B1, we see a very good match, showing that GIZMO resolves the linear growth in the expected way, although the nonlinear results are not perfect exponentials due to the noise inherent in the meshless method of GIZMO (fluctuation amplitudes remain small at this time, so the noise makes a relatively larger contribution). Similar results from LsmallNd1 are shown in Fig. B2. The converged linear growth rates of these parallel modes ($\theta_k = 0$) are effectively zero for all modes, $k > 12 \times 2\pi/L$, that fit in the box. In order to assess convergence we plot the linear prediction given different discretizations in dust size space, as discussed in App. A3.2. Although the linearly predicted growth rates are very slow even for $N_d = 1$, and so are hard to tell apart in the somewhat noisy numerical data, the simulation results show no indication of linear growth and thus appear inconsistent with linear predictions for $N_d \leq 4$. Given that this simulation is discretized with one dust particle per gas particle, this is reasonable evidence that the key physics of the continuous grain spectrum is being resolved by our method.

It has proven somewhat more difficult to assess the convergence of the growth rate for the overlapping quasi-resonant “forward quasi-sound modes” at these parameters, although we clearly see nearly perpendicular modes growing strongly in large dust grains in both the high-resolution main-text simulation (see Fig. 4) and the LsmallNd1 simulation, and these broadly match the predicted growth rates. We speculate that the difficulty of measuring the detailed mode structure relates to its relative narrowness in θ_k and the influence of the remeshing noise. Given the strong sensitivity of even the linear results to k and N_d , a detailed study of the linear growth of these modes would require other simulations with careful convergence checks in N_d and k , and is beyond the scope of this work (see Krapp et al. 2019; Paardekooper et al. 2021; Zhu & Yang 2021). In Fig. B3, we show the growth rate as a function of θ_k and k , measured from the non-constant-drift simulation of the main text for $t \leq 3$. The agreement with linear predictions is good for quasi-parallel modes, and reasonable for quasi-perpendicular modes, most of which grow around the linearly predicted rate (note that for a given k , modes exist only for certain θ_k due to the grid, which makes it hard to resolve the fine structure). Given the uncertainties in the measurement method – different modes can interact, and the simulation is somewhat noisy in this low-amplitude initial phase – the overall agreement is reasonable, and justifies the ability of GIZMO to resolve the mode structure of the polydisperse acoustic RDI.